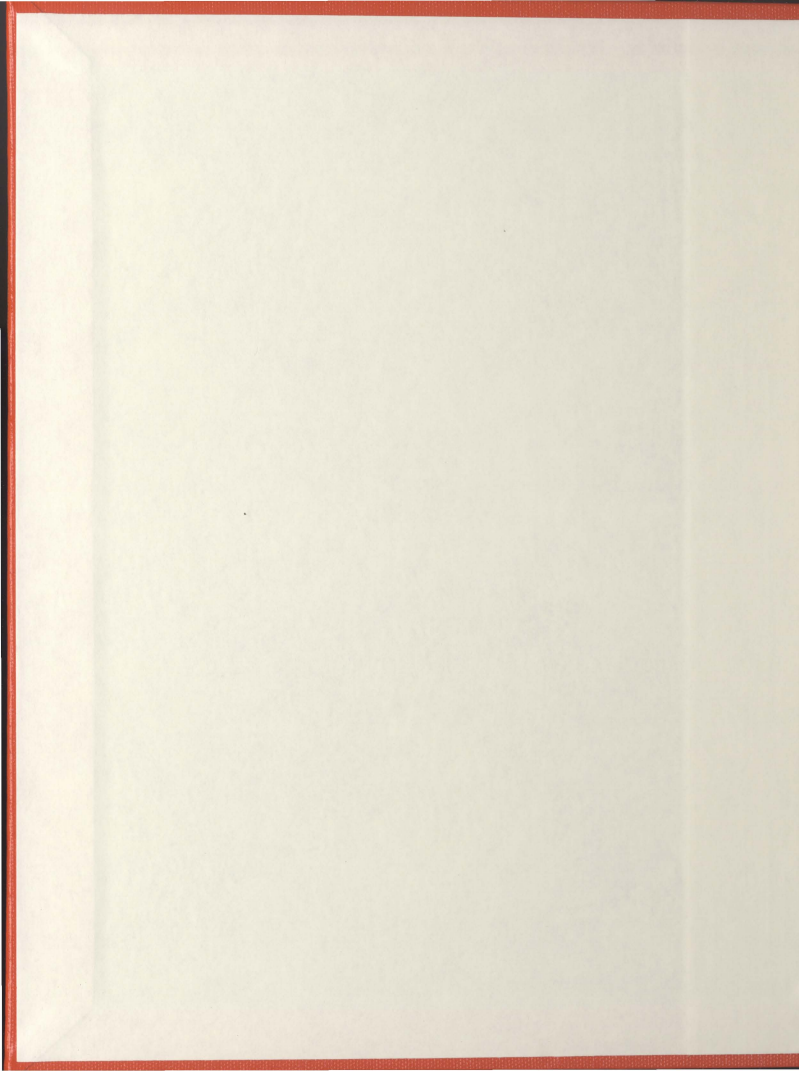


AN ALGORITHM FOR THE EXTRACTION OF
OCEAN SURFACE CURRENT VELOCITY FROM
BISTATIC HF GROUNDWAVE RADAR DATA -
A SIMULATION

QIU JIN



An Algorithm for the Extraction of Ocean Surface
Current Velocity from Bistatic HF Groundwave
Radar Data — A Simulation

by

©Qiu Jin, B.Eng.

A thesis submitted to the School of Graduate Studies
in partial fulfillment of the requirements for the
degree of Master of Engineering

Faculty of Engineering and Applied Science
Memorial University of Newfoundland

May, 2007

St. John's

Newfoundland



Abstract

More than seventy percent of our earth surface is covered by ocean. The conditions at sea will not only influence our climate, but also affect human activities such as off-shore oil drilling, fisheries, etc.. Monitoring ocean surface information, such as surface current, wave and wind conditions, becomes more and more important. High frequency (HF) ground wave radar is proven to be a very useful tool for measuring ocean surface current. The ability of the HF signal to travel beyond the line-of-sight because of the high conductivity of seawater enables the radar to be used to survey and obtain the ocean surface current maps over a large ocean area. The longer radio wavelength also allows measurements to be conducted under all weather conditions. In addition, the features of near real-time measurement and high spatial and temporal resolutions make this method more attractive than conventional techniques, such as are available from surface current meters and drifter buoys.

The component of the current velocity along the radar look direction can be extracted from the first-order Doppler shift of the electromagnetic wave scattered from the ocean surface. In order to obtain a current vector, at least two projections along different directions should be known. This can be achieved by two widely separated monostatic radar installations, each of which contains a co-located transmitter and receiver. Another, potentially more cost effective, approach is by means of a pair of bistatic and monostatic receivers sharing the same radar transmitter. In this configuration the projections of the current along two different directions can be found and thus the current velocity can be obtained without significantly losing potential coverage. Here, an algorithm is developed to examine the relevant issues of this new approach of surface current measurements. More specifically, the scatter patch in this model is chosen to be along a constant bistatic angle curve. The simulated bistatic and monostatic radar received time series data are

processed by averaging fifteen 512-point fast Fourier transforms with 50 percent overlap to yield the Doppler spectrum (power spectral density (PSD)). The first-order Doppler shifts are obtained by comparing the centroid frequencies of the spectral peak regions with their theoretical positions determined by the Bragg scatter mechanism. The current components are obtained from these Doppler offsets. The error analysis is carried out by means of the concept of geometric dilution of precision (GDOP).

While no consideration is given to the significant problem of sidelobes in the antenna patterns, zero-mean Gaussian noise from external sources is added to simulate pulsed HF radar clutter from the ocean surface. Deep water is assumed when the monostatic and bistatic radar data are simulated. The combination of clutter PSDs and noise makes the simulated radar data more realistic.

Acknowledgements

The author wishes to express her sincerest thanks to the Faculty of Engineering and Applied Science, Memorial University of Newfoundland, St. John's, Canada for giving her this opportunity of conducting this work. Particularly, the suggestions and guidance of the author's supervisors, Dr. Eric W. Gill and Dr. John Walsh, are greatly appreciated.

Thanks are also owed to author's colleagues and friends, in particular Weimin Huang, for their help and assistance on computer programming and other aspects at various stages of the work.

The work could not have been completed without graduate student support from Natural Science and Engineering Research Council (NSERC) grants to Dr. Eric Gill and Dr. John Walsh.

The patience and understanding of the author's husband Jianjun Zhang and lovely son Zhipu Zhang are also appreciated.

Contents

Abstract	iii
Acknowledgements	iv
Contents	v
List of Figures	vii
List of Tables	xi
Table of Symbols	xii
Table of Abbreviations	xvi
1 Introduction	1
1.1 General Information	1
1.2 Literature Review	4
1.3 Scope of Research	10
2 Principles of HF Radar Current Measurement	13
2.1 The Scattering Mechanism	14
2.2 Radial Current Measurements	18
2.3 Vector Current Derived from Monostatic Radar	19

2.3.1	Single-site Approach	19
2.3.2	Dual-site Approach	21
2.4	Bistatic Configuration with Constant Bistatic Angle	22
2.5	From Radial Currents to Vector Current	26
3	Error Analysis	29
3.1	Errors in Radial Current Measurements	29
3.2	Errors in Vector Current Combination	31
4	Vector Current Extraction from Simulated Bistatic Data	41
4.1	Review of Cross Sections	42
4.1.1	Directional Ocean Wave Spectra	42
4.1.2	First-order Cross Section	45
4.1.3	Second-order Cross Section	48
4.1.4	Simulation of Cross Sections	51
4.2	Time Series of Radar Return	57
4.2.1	The PSD of Ocean Clutter	58
4.2.2	The PSD of Stationary Gaussian Noise	60
4.2.3	The Simulated Time Series	61
4.3	From Time Series to Vector Current	62
4.3.1	Introduction	62
4.3.2	Simulation Details	65
4.3.3	Simulated Results for Uniformly Distributed Currents	67
4.3.4	Simulated Results for Non-uniform Current Pattern	70
5	Conclusions	82
5.1	General Summary	82
5.2	Suggestions for Future Work	84

List of Figures

2.1	The general geometry of the bistatic configuration.	17
2.2	The simulated radar Doppler spectrum (power spectral density, PSD) with zero-mean stationary Gaussian noise. The radar operating frequency is 15 MHz, the bistatic angle is 55° , and the wind speed is 10 m/s, 75° to the x -axis.	20
2.3	Locus of constant bistatic angle.	23
2.4	The geometric relationship of the bistatic and monostatic radar look directions with bistatic angle of ϕ_0 . T , R_m and R_b represent the transmitter and monostatic and bistatic receivers, respectively.	24
2.5	The current vector is obtained from the combination of the radial current components, V_m and V_b	27
3.1	Geometrical relation of the current components.	32
3.2	The plot of GDOP against the intersection angle (dashed line). The solid line indicates a threshold of GDOP as an example. The GDOP values that exceeds the threshold will be discarded.	34
3.3	The maximum errors in magnitude and direction when the bistatic angle changes from 0° and 90° . The input current is 0.6 m/s, 60° to the x -axis. The errors in monostatic and bistatic radar look directions are 4.5 cm/s and 5 cm/s, respectively.	36

3.4	The maximum errors in magnitude and direction as a function of the intersection angle (bistatic angle) when a vector current is measured by an HF radar system with monostatic and bistatic receivers. The current is 0.6 m/s, 60° to the x -axis.	37
3.5	The maximum errors of the current magnitude and direction when two radar receiver beams are 30° and 75° to the x -axis (the bistatic angle is 45°). The magnitudes of currents are 0.3 m/s, 0.6 m/s, and 1.2 m/s, respectively. The FFT resolutions in both directions are 4 cm/s.	38
3.6	The same as Figure 3.5, except the FFT resolutions in two directions are 4 cm/s and 6 cm/s, respectively.	39
3.7	The predication of changing range. A set of vector currents are with speeds 0.8 m/s, and in the directions of 10°, 40°, 70°, 100°, and 130°, respectively. The two radar look directions are 30° and 75°. All angles are with respect to x -axis.	40
4.1	Pierson-Moskowitz ocean wave spectra as functions of wind speed and wavenumber.	45
4.2	The two sections of the bistatic first-order cross section with ($m = \pm 1$) indicates the positive and negative Doppler portions. The bistatic angle is 30°. The wind velocity is 15 m/s, perpendicular to the radar look direction.	47
4.3	An enlarged view of the second-order scattering relations for the bistatic patch scattering.	48
4.4	The four sections of the bistatic second-order cross section. The radar operating frequency is 25 MHz, the bistatic angle is 30°, the wind velocity is 15 m/s perpendicular to the radar look direction. Only the $K_1 < K_2$ case is simulated here.	49
4.5	Bistatic cross sections for a wind speed of 15 m/s with different wind directions of $\theta_w = 0^\circ, 45^\circ, 90^\circ, \text{ and } 135^\circ$, respectively. The bistatic angle $\phi_0 = 45^\circ$ (see Figure 2.4) and the radar operation frequency $f_0 = 15$ MHz.	52

4.6	Bistatic cross sections for wind speeds of 10 m/s (left) and 15 m/s (right) with wind direction 0° to x -axis. The radar operating frequency is 15 MHz and the bistatic angle is 45°	53
4.7	Bistatic cross sections for different radar frequencies. The bistatic angle is $\phi_0 = 45^\circ$. The wind velocity is 10 m/s, 0° to x -axis.	55
4.8	Bistatic cross sections for different bistatic angles. The radar operating frequency is 15 MHz, wind velocity is $u_w = 10$ m/s, 0° to the x -axis.	56
4.9	A pulse train with pulse width τ_0 and pulse repetition frequency T_L	59
4.10	Power spectral density of external noise.	61
4.11	Example of radar received time series. Radar operating frequency is 25 MHz, wind velocity is 15 m/s, 90° to radar look direction.	63
4.12	An illustration of cell number.	66
4.13	An example of radial currents measured from monostatic and bistatic radar directions. The radar operating frequency is 25 MHz, the bistatic angle is 55° , and the location of the ocean surface is at cell number four. The original current is 1.2 m/s, 60° to the reference direction. The dotted lines indicate the centroid frequencies of the Bragg peaks without the current, while the dashed lines show the Doppler shifted centroid positions of the Bragg peaks.	68
4.14	Results for different current magnitudes measured at 25 MHz. The bistatic angle is 25° . The magnitudes are selected as 0.15 m/s, 0.3 m/s, 0.6 m/s, 0.9 m/s, and 1.2 m/s. The current direction is 60° to the x -axis.	69
4.15	Results for currents with different magnitudes measured at 25 MHz. The bistatic angle is 30° . The other parameters are the same as in Figure 4.14.	69
4.16	Absolute differences of the radial current components along the monostatic and bistatic directions measured at bistatic angle of 25° . The parameters are the same as in Figure 4.14.	71

4.17 Absolute differences of the radial components along the monostatic and bistatic directions measured at bistatic angle of 30° . The parameters are the same as in Figure 4.15. 72

4.18 A current with 0.9 m/s, 60° to the x -axis is measured. The radar frequency is 25 MHz, bistatic angles are 25° , 35° , 45° , and 55° , respectively. 73

4.19 Same current as in Figure 4.18 is measured. The radar frequency is 6.75 MHz. The bistatic angles are chosen as in Figure 4.18. 73

4.20 The comparisons of original current maps and current maps simulated at 25 MHz, 15 MHz, and 6.75 MHz, respectively. 75

4.21 The absolute errors in (a) magnitude and (b) direction for the simulated currents at a bistatic angle of 55° . The radar operating frequencies are 25 MHz, 15 MHz, and 6.75 MHz, respectively. 76

4.22 The absolute errors in (a) magnitude and (b) direction for the simulated currents at a bistatic angle of 45° . The radar operating frequencies are the same as in Figure 4.21. 77

4.23 The absolute errors in (a) magnitude and (b) direction for the simulated currents at a bistatic angle of 35° . The radar operating frequencies are the same as in Figure 4.21. 78

4.24 The absolute errors in (a) magnitude and (b) direction for the simulated currents at a bistatic angle of 25° . The radar operating frequencies are the same as in Figure 4.21. 79

List of Tables

4.1	Maximum errors in current magnitude.	80
4.2	Maximum errors in current direction.	80

Table of Symbols

(The page numbers in the symbol definitions indicate the place of first mention.)

- f_B : Doppler frequency of Bragg peaks (p. 7).
- g : Acceleration due to gravity (p. 7).
- k_0 : Radar radiation wavenumber (p. 7).
- ϕ_0 : Bistatic angle (p. 7).
- σ_1 : First-order bistatic cross section (p. 7).
- σ_{2P} : Second-order bistatic cross section of patch scatter (p. 7).
- σ_{2T} : Second-order bistatic cross section when one of the scatters occurs at the ocean surface near the radar transmitter (p. 7).
- σ_{2R} : Second-order bistatic cross section when one of the scatters occurs at the ocean surface near the radar receiver (p. 7).
- λ_0 : Radio wavelength (p. 8).
- ω : Radian frequency of an ocean wave (p. 14).
- K : Ocean wavenumber (p. 14).
- v_p : Phase velocity of ocean wave (p. 14).
- λ : Wavelength of ocean wave (p. 15).
- θ : Incidence angle (p. 15).
- ω_B : Doppler radian frequency of Bragg peaks (p. 16).
- f_0 : Radar frequency in megahertz (p. 16).
- T : Radar transmitter (p. 16).
- R_b : Bistatic radar receiver (p. 16).
- P : Scatter patch (p. 16).
- \hat{N} : Unit normal to the scattering ellipse (p. 17).

- θ_m : Direction of monostatic radar look direction (p. 17).
- θ_N : Direction of \hat{N} (p. 17).
- Δf : Different Doppler shift between measured and theoretical Bragg peaks (p. 19).
- V_r : Radial component of ocean current velocity along radar look direction (p. 19).
- f'_B : Measured Bragg peaks (p. 19).
- R_m : Monostatic radar receiver (p. 22).
- θ_b : Angle between bistatic receiving direction and reference direction (p. 24).
- ρ_{01} : Distance between transmitter and scatter patch (p. 24).
- ρ_{02} : Distance between scatter patch and receiver (p. 24).
- d : Half distance between transmitter and bistatic receiver (p. 24).
- (x, y) : x, y components of scatter patch in Cartesian coordinate system (p. 26).
- V_c : Magnitude of the surface current (p. 27).
- θ_c : Direction of the surface current (p. 27).
- V_m : Projection of current vector along the monostatic radar look direction (p. 27).
- V_b : Projection of current vector along the bistatic radar look direction (p. 27).
- Δv_r : Radial current resolution (p. 30).
- λ'_0 : Modified radar operating wavelength (p. 30).
- V_1, V_2 : Measured radial currents along two radar look directions (p. 31).
- α, β : Angles of V_1 and V_2 with respect to the reference direction (p. 31).
- ϕ : Intersection angle of two radar look directions (p. 32).
- u, v : Two orthogonal components of current vector (p. 32).
- σ_1, σ_2 : Standard deviations along V_1 and V_2 directions (p. 33).
- σ_v, σ_u : Standard deviations along u and v directions (p. 33).
- σ : Standard deviations along the vector current (p. 33).

- Va, Vb, Vc, Vd, Ve, Vf : Vector current along various directions
of $10^\circ, 40^\circ, 70^\circ, 100^\circ$, and 130° , respectively (p.40).
- $S_1(\vec{K})$: Directional ocean wave spectrum (p. 42).
- $S_1(K)$: Non-directional ocean wave spectrum (p. 42).
- $\theta_{\vec{K}}$: Dominate directional of ocean wave (p. 42).
- $g(\theta_{\vec{K}})$: Directional factor of ocean wave spectrum (p. 42).
- $S_{PM}(K)$: Pierson-Moskowitz spectrum (p. 43).
- α_{PM} : A constant with value 0.0081 (p. 43).
- u_w : Wind speed measured at 19.5 m above the ocean surface (p. 43).
- $s(K)$: Spread function (p. 43).
- $\bar{\theta}(K)$: Mean wind direction (p. 43).
- θ_w : Wind direction with respect to the reference direction (p. 44).
- $\Delta\rho_s$: Scattering patch width (p. 45).
- $Sa(\cdot)$: Sampling function (p. 45).
- c : Free space speed of light ($= 3 \times 10^8$ m/s) (p. 46).
- τ_0 : Pulse width in time (p. 46).
- K_{Bbi} : Bragg peak wavenumber for bistatic scattering (p. 47).
- K_{Bmono} : Bragg peak wavenumber for monostatic scattering (p. 47).
- $\delta(\cdot)$: Dirac delta function (p. 49).
- $s\Gamma_P$: Symmetric coupling coefficient (p. 50).
- $H\Gamma_P$: Hydrodynamic coupling coefficient (p. 50).
- $E\Gamma_P$: Electromagnetic coupling coefficient (p. 50).
- P_c : Doppler power spectral density of ocean clutter (p. 58).
- T_L : Pulse repetition period (p. 58).
- P_t : Transmitter peak power (p. 58).
- G_t : Radar transmitter gain (p. 58).

- G_r : Receive array gain (p. 58).
 $F(\cdot)$: Rough spherical earth attenuation function (p. 58).
 A_r : patch area (p. 58).
 $BW_{\frac{1}{2}}$: Half-power beam width of radar receiver (p. 58).
 d_s : Spacing between antenna array elements (p. 59).
 P_N : Noise power spectral density (p. 60).
 $k = 1.38 \times 10^{-23} \text{ J/K}$: Boltzmann's constant (p. 60).
 $T_0 = 290 \text{ K}$: Reference temperature (p. 60).
 F_{am} : External noise *figure* (p. 60).
 d_c : Radar duty cycle $\frac{T_0}{T_L}$ (p. 60).
 B : Receiver bandwidth (p. 61).
 $f(t)$: Time series of ocean wave signal (p. 61).
 $c(t)$: Ocean clutter signal (p. 62).
 $n(t)$: Noise voltage as observed by a pulse radar (p. 62).
 $s(t)$: Summation of $c(t)$ and $n(t)$ (p. 62).

Table of Abbreviations

(The page numbers in the symbol definitions indicate the place of first mention.)

- HF: High frequency (p. 1).
- NOAA: National Oceanic and Atmospheric Administration (p. 8).
- CODAR: Coastal Ocean Dynamics Applications Radar (p. 8).
- WERA: Wellen Radar (p. 8).
- FMCW: Frequency modulated continuous wave (p. 8).
- FFT: Fast Fourier transform (p. 8).
- MCR: Multi-frequency coast radar (p. 8).
- OSCR: Ocean surface current radar (p. 8).
- NRI: Northern Radar Incorporated (p. 8).
- PSD: Power spectral density (p. 20).
- SNR: Signal to noise ratio (p. 29).
- GDOP: Geometric dilution of precision (p. 31).
- GSP: Global Positioning System (p. 31).

Chapter 1

Introduction

1.1 General Information

Being driven by geotropic forces and tides, ocean surface current is strongly affected by such factors as the water's salinity, the local surface wind and wave, and the earth's rotation. Ocean water is constantly moving and the movement of water also acts as a carrier that transports floating matter such as surface borne pollutants, fish larvae, and spilled oil. Therefore, ocean surface current information is highly valuable in offshore development, search and rescue, and scientific research. Listed below are a few examples that highlight this fact:

1. A knowledge of surface currents is essential for the design of offshore structures.
2. It is more efficient to detect and track the trajectories of targets for search and rescue applications by estimating the current velocity.
3. Spilled oil and other surface-borne pollutants can be tracked based on the current information.
4. Current information may provide better knowledge of fish larvae transport, which

affects the coastal fishery management.

5. A database containing the long-term current measurement may help in predicting iceberg tracks.

Current can be measured by conventional oceanographic instruments such as current meters and drifters, but these devices may provide the current information over limited regions of ocean and time periods. Moreover, when using conventional approaches, there may be restrictions. Current meters, for instance, must be moored below a certain depth to avoid interference with ship and damage by ice, and, in fact, surface current values may be different from those obtained at the moored locations. However, radio oceanographic techniques for remote sensing provide an effective and reliable means to measure ocean surface current and provide valuable input in satisfying these coastal management requirements.

Shearman [1] gives a good introduction to the remote sensing of the ocean surface by radio techniques. These techniques include microwave radiometry, microwave radar, and high frequency (HF) radar. Microwave radar can be used to provide some ocean surface parameters with the line-of-sight limitation. However, the measurements obtained are more likely to be affected by the weather condition and sophisticated sensors may be needed. Furthermore, microwaves mainly interact with ocean waves with short wavelength while the significant ocean energy is found in the much longer gravity wave. It is a complicated indirect process for microwave radar to obtain the information of these long waves by means of their modulation effects on the short waves.

On the other side, the wavelengths of HF electromagnetic radiation are of the same order of magnitude as those ocean gravity waves which carry most of the ocean energy. Thus the HF radar wave may interact strongly with these ocean waves. It is also well known that ocean water is a good conducting medium in the HF band. Guided by this medium, the transmitted radar signals in the HF frequency band (from 3 MHz to

30 MHz) will travel along the earth's curvature and reach far beyond the line-of-sight. From the returning signals, plenty of ocean surface information, including ocean surface current vectors, may be extracted. Over the past two decades, HF radar, operating in both sky wave and ground wave modes, has been successfully used to measure ocean surface characteristics. The potential surveillance of large extents of the ocean surface over long time periods makes this technique very attractive.

In spite of the high initial installation cost, there are numerous advantages in using HF radio technology for current measurement. Listed below are some of the advantages:

1. Extraction of surface currents from HF radar can be performed over a range of 400 km and an area of many thousands of square kilometers in nearly real-time, while the conventional current measurements are basically a snapshot over the ocean surface with limited range and coverage.
2. Because of the longer wave-length of electromagnetic waves, HF radar is not affected by precipitation and is able to be operated in any weather conditions.
3. It is virtually impossible to produce fine-resolution current maps by conventional methods. However, when two HF radars survey a common coverage area, current maps with high resolution may be produced. A database for the measurements with fine spatial and temporal resolutions can be developed by gathering long term time series.
4. In conventional current measurement, there is a considerable cost associated with data collection, since data is collected by aircraft, ships, or satellites. Management requirements are minimized by using HF radar.

1.2 Literature Review

The interaction between electromagnetic waves and the ocean surface was first treated as noise when radar was used to detect targets such as ships and boats. Considerable effort was expended in trying to remove this so-called clutter. Crombie [2] initially performed experiments for measuring the ocean surface features by spectrally analyzing the returned radar signal. He concluded that the sea surface behaves like a diffraction grating and the Bragg mechanism is responsible for the scatter. The Bragg scattering mechanism, as will be discussed theoretically in Chapter 2, indicates that the dominant contribution to the sea clutter is produced by scatter from the ocean waves having a wavelength half that of the radar wavelength, and moving radially toward and away from the radar site if monostatic configuration is assumed. This first-order resonant phenomenon results in two peaks in the Doppler frequency domain. The peak positions indicate the radial speed of the resonant wave components. Crombie also noticed that the Bragg peaks in the returned Doppler spectrum were subject to a small frequency shift from their positions predicted by the dispersion relationship for water waves. He postulated that the small shift could be the consequence of the motion of the entire water surface. He also proposed that the ocean surface current may be measured routinely by a properly configured HF radar. Subsequent research and experiments [3, 4] have verified Crombie's idea of surface current measurement. To date, more than one hundred HF radar systems have been installed for extracting ocean surface current and other information in North America, Europe, Australia, and more recently in Asia.

To describe the fundamental mechanism of the "radar wave-ocean wave" interaction, the scattering cross section needed to be developed. The formal definition of the radar cross section is "that area which, when multiplied by the power flux density of the incident wave, would yield sufficient power that could produce by isotropic radiation, the same radiation intensity as that in a given direction from the scattering surface" [5].

The developed HF radar cross sections include first-order and higher order parts. They are influenced by radar operating frequency, beam form, configurations (monostatic or bistatic), and the polarization of transmitted electromagnetic wave. They are also functions of sea surface states, which concern wind velocity, surface roughness, etc..

Barrick [6] was the first to derive the HF radar cross sections of the ocean surface. Beginning from Rice's perturbation theory [7], Barrick formulated a first-order scattering cross section based on the assumptions of a plane electromagnetic wave with grazing incidence and vertical polarization, and a time-varying ocean surface with a good, but finite surface conductivity. In the same year, Barrick [8] also developed a theoretical non-linear, two-dimensional Fredholm-type integral equation for the second-order backscatter cross section which partially explained the continuum surrounding the first-order peaks. The integrand in the formulation contains the second-order electromagnetic and hydrodynamic coupling coefficients. These coefficients correspond to the different interactions between radar signals and water waves and between water waves themselves. The non-linear factor in the integrand originates from the product of two ocean wave directional spectra. Barrick and Lipa [9] further produced another set of expressions to account for shallow water effects. However, the cross sections derived by Barrick are primarily for the case of co-location of transmitter and receiver, i.e. for the monostatic configuration.

Walsh [10] has formulated a generalized-function approach to the scattering of electromagnetic fields from the boundary of two different media. A step function is used to characterize the change in constitutive parameters from one medium to another. Based upon Walsh's generalized-function approach, Srivastava [11] obtained expressions for the first- and second-order monostatic cross sections. Among the three parts of second-order cross sections in Srivastava's expression, the first part is denoted as the patch scatter term and is seen to be equivalent to Barrick's model [8]. It is this on-patch scatter part, involving a double scatter on a single patch of ocean that is far from the radar

station, that dominates the second-order cross section. The other parts can be viewed as two separate interactions of the transmitted signal with two widely separated patches of the surrounding ocean surface. The successful model developed by Walsh's *et al.* [12] similarly includes higher-order backscatter effects.

Regardless of the radar configuration model, monostatic or bistatic, Walsh and his colleagues (Srivastava, Howell, Dawe, and Gill) attacked the same cross section problem under the same assumptions as Barrick [6] but with a pulsed radar waveform [12, 13]. This makes the cross sections more realistic because the finite pulse corresponds to a finite scatter patch on the ocean surface. By examining the fields of a pulsed dipole source scattered from the finite patch, their cross section expressions depict the Bragg scatter as a squared sampling function, which is like a smeared or widened delta function. Examination of the cross sections from real data indicates that the cross section models based on Walsh's formulation successfully describe the interactions between the radio wave and the ocean wave.

Gill and Walsh's bistatic first- and second-order radar cross sections [13] are among the most recent significant developments in this area. In the bistatic radar configuration the transmitter and receiver are widely separated (i.e. not co-located). This analysis is based on Walsh's [10] generalized-function approach and provides a more general cross section model. It is obvious from these models that the monostatic result is a special case of bistatic cross section model with the bistatic angle set equal to zero. Our studies on current measurement are based on the bistatic radar configuration. When the algorithm is addressed in Chapter 2 the advantages of the bistatic model will be summarized. There also a detailed introduction to Gill and Walsh's [13] bistatic cross section model is presented. The simulation of the Doppler spectra from the cross sections for both monostatic and bistatic models will be shown in Chapter 4.

In Gill and Walsh's bistatic cross section model, the first-order peaks are modeled

by a squared sampling function. The locations of the Bragg peaks are at the Doppler frequencies of $f_B = \pm \frac{1}{2\pi} \sqrt{2gk_0 \cos \phi_0}$ if deep water is assumed. In this equation, g is the acceleration due to gravity, k_0 is the wavenumber of radar and ϕ_0 is bistatic angle. The bistatic angle is defined as one-half of the angle between radar transmitter and receiver as viewed from the scatter points. There are three parts in the total second-order cross section, corresponding to three kinds of scattering over the ocean surface. They are denoted as σ_{2P} , σ_{2T} and σ_{2R} . σ_{2P} , denoted as patch scattering, is scatter in which the scatters occur at the ocean surface far from the transmitter and receiver; σ_{2T} corresponds to the scatter in which one of two scatters occurs at the ocean surface near the radar transmitter; and σ_{2R} accounts for the scatter in which one of the scatters is near the radar receiver. Thus, the total cross section, given by Gill and Walsh [13] and Gill *et al.* [14], contains four components: one first-order component and three second-order components. Among the three second-order components the patch scatter σ_{2P} is dominant, which is similar to Srivastava's monostatic results [11]. For simulation purposes in Chapter 4, we take the patch scattering case into consideration and neglect the other two components in the second-order cross sections as they do not affect the measurement of the ocean current.

Another significant contribution given by Gill [15] is that the external noise in the radar returns is taken into consideration. In his model, based on the assumption of a pulsed radar system and a typical noise regime, time series of radar received ocean clutter have been simulated to achieve a more realistic result. In our research, as in Gill's model, zero-mean Gaussian white noise will be considered.

Interest in using HF radar for ocean surface current measurements has been increasing in the past three decades. A number of experiments have been successfully conducted. In accordance with Crombie's assertion of HF radar current measurement, Stewart and Joy [3] conducted two experiments in January and May of 1973 off San Clemente Island

in the Pacific Ocean near California. They compared the radar-deduced current with conventional measurements of the same current and concluded that the current measured by radar is actually an average of surface currents over a depth of $\lambda_0/8\pi$ where λ_0 is the radio wavelength. At the same time, Barrick *et al.* [4] performed a similar experiment and arrived at the same conclusion. These successful experiments provided an important foundation for measuring surface current by HF radar.

In 1977, the National Oceanic and Atmospheric Administration (NOAA) developed the first coastal radar system, Coastal Ocean Dynamics Applications Radar (CODAR), that has the ability of mapping surface currents [16]. The receiving antenna of the first CODAR system is a four-element monopole antenna. The advantage of this system is that it is a small compact system. However, it has the potential failure of ambiguity and cannot access information on the second-order backscatter because of the employment of the non-directional antennas. This CODAR system has been improved and now the up-to-date equipment, SeaSonde, is available as one of a few commercial HF radar systems around the world. With a portable antenna, the SeaSonde can measure current up to 70 km. As another successful commercialized HF radar current measurement system, the Wellen Radar (WERA), was developed by a research group in University of Hamburg [17]. The WERA system has an antenna array depends on the radar frequency and the number of elements in the array. A large space, typically on the order of 100 m in length, near shore is needed to install WERA system. It is thus able to acquire backscatter information from a selected ocean surface patch. WERA uses a frequency modulated continuous wave (FMCW) as the transmitting waveform. It has the advantage of the flexibility in range resolution between 0.3 km to 1.2 km. However, when using FMCW, two fast Fourier transforms (FFTs) are needed; the first FFT is applied to resolve the range and the second FFT is applied to obtain the Doppler spectra.

Other HF radar systems have been built for specific purposes. For example, multi-

frequency coast radar (MCR), developed by the University of Michigan [18], is a pulsed radar that can be operated simultaneously with frequencies of 4.8 MHz, 6.78 MHz, 13.48 MHz, and 21.77 MHz. It is able to measure not only the surface current but also the vertical structure of the current in the top 2.5 m of the ocean surface. Also, the ocean surface current radar (OSCR), originally developed at UK Rutherford and Appleton Laboratories [19], can be used in both HF and VHF bands for the ocean surface measurement. This system employs a 16-element phase array antenna to achieve narrow beam in the HF band and a 32-element phased array in VHF band. The VHF mode of OSCR was well demonstrated as an ocean sensor in an experiment in South Florida [20].

One of the first experiments for the purpose of current measurement in Canada was conducted in 1983 by using CODAR's radar at sites in Cape Race and Cape Cappareyden, NL [21]. Current maps were successfully obtained. Since then, many experiments have been conducted in the measurement of not only surface current, wave, and wind parameters but also in the detection and tracking of ships, low-flying aircrafts, and ice. In the fall of 1990, a new multi-purpose, long-range shore based ground wave radar system was set up in Cape Race, NL, by a local company, Northern Radar Systems Limited (NRS�), now Northern Radar Incorporated (NRI). This long range radar system with steerable narrow-beam was able to survey a range of up to 400 km over a 120° sector of the ocean surface, for a maximum coverage area of more than 160,000 km². To demonstrate the ability of this state-of-the-art long-range system as a current measurement facility, a single-station current measurement model has been developed by Hickey [22] using standard regression techniques.

Bobby's dual-site approach [23] is based on two spatially separated radar facilities located in Cape Race and Cape Bonavista that cover a common ocean surface off the coast of Newfoundland. The radial currents are derived from each set of radar data and the vector current is established through geometric manipulations. Bobby also extends

the estimation of surface current beyond the region of overlap area by implementing of the continuity equation proposed by Frisch and Leise [24].

When using HF radar to measure ocean surface currents, spatial resolution in both azimuth and range must be considered. Different techniques have been applied in different systems. The azimuthal resolution depends on the beam form of the receiving antenna. There are mainly two kinds of techniques to achieve it, direction finding and beamforming. The direction finding technique, performed in the frequency domain, involves calculating complex Fourier transform of the time series, while beamforming is performed in the time domain by adding the weighted and phase-shifted signals of all antennas. The CODAR system [16] is an example of the direction finding model. The WERA Radar, on the other hand, uses the beamforming model to provide measurements of ocean surface current and the wave directional spectrum.

1.3 Scope of Research

HF radar has been used for oceanographic measurements for nearly three decades and the techniques are still developing steadily. However, in the existing HF radar ocean current measurement systems, such as CODAR, MCR, WERA, OSCAR, and radar systems operated by NRI, the algorithms for deriving ocean surface vector current are all based on the monostatic radar configuration. With the introduction of the bistatic radar cross section by Gill and Walsh [13], it is feasible to install a HF radar current measurement system as a combination of monostatic and bistatic radar configurations. This system contains a full radar system with transmitter and receiver co-located and another radar receiver separated tens of kilometers from the transmitter. Radial current components from the two receivers are recorded and analyzed independently. The vector current can be derived from the radial current components. The motivation for this work is to develop a new algorithm for this combined radar current measurement system. The scatter patch

will be defined along a path with a constant bistatic angle. In spite of the complicated algorithm due to combination of two configurations, there are several advantages that make this study valuable. One advantage of using this combined radar system is the effective cost saving compared with dual-site model, because only one transmitter is required for the two-receiver system. In fact, potentially this transmitter can be shared by several different receivers. Thus, a significant expansion in the radar coverage may be achieved.

In this thesis, when the algorithm of the combined method is introduced, it is assumed that the receiving antennas in both monostatic and bistatic configurations are narrow-beam. With the aid of the bistatic model developed by Gill and Walsh [13], the radar data from both receivers will be simulated and the radial current components will be derived along each receiver look direction. The overall vector current will be obtained from these two radial currents. Additionally, the errors throughout the whole process will be analyzed numerically. They include the errors in obtaining radial current components and those in the procedure of radial combination to produce the vector currents. The latter error is related to the geometric relationship involving both receiving antennas and the scattering patch.

Chapter 1 serves as a general introduction to radio oceanography and the development of HF radar cross sections. It also includes a brief discussion of the history of HF radar as a tool of ocean surface current measurement. Chapter 2 explains the physical mechanism involved in the use of HF radar as a remote sensor for ocean surface information. Determination of the ocean surface current from single or dual radar sites will be introduced. The geometric relationship of the combined configuration mentioned above will be presented. Chapter 3 provides an analysis of the errors in both radial current and vector current derived from radar data. Chapter 4 presents the simulated results of the current vector detection. In this chapter, the bistatic cross section will be introduced

based on Gill and Walsh's model [13]. As already noted, the monostatic scatter will be viewed as a special case of bistatic scatter when the bistatic angle is equal to 0° . The first- and second-order cross sections for bistatic configuration will be simulated for different sea states, radar frequencies, and bistatic angles. Different current vectors, as well as a white Gaussian noise with zero mean will be added to the radar received signal. Finally the radial current and vector current will be extracted from simulated HF radar data. Chapter 5 briefly concludes the studies and gives suggestions for future work.

Chapter 2

Principles of HF Radar Current Measurement

As noted in Chapter 1, Crombie [25] first proposed that the mechanism responsible for large peaks at specific frequencies in HF sea echo is Bragg scattering. He further hypothesized that Doppler spectral shifts in these peaks from their theoretical positions could be explained by the presence of ocean currents. The research and experiments following Crombie's assumption proved that the radar return signal contained important information about the ocean surface. This information includes surface current, wave parameters, and wind field. This chapter will give a detailed explanation of the Bragg scattering mechanism, the relation between Doppler shift and radial current, the configuration of bistatic and monostatic receivers with respect to the scattering patch, moving along the locus of constant bistatic angles, and the trigonometric manipulation of two radial currents along different directions to produce a vector current.

2.1 The Scattering Mechanism

Before examining the actual mechanism, we first consider a few relevant features of ocean waves. Ocean surface waves can be categorized as capillary or gravity waves according to their restoring forces [26]. Capillary waves are those whose restoring force is dominated by the effects of surface tension. Capillary waves have a wavelength of a few centimeters and waveheight of a few millimeters. They form a remarkably regular diamond-shaped pattern and wrinkle the ocean surface much more than large waves. When the wavelengths of ocean waves are longer than about 1.73 cm, they are no longer purely capillary waves but becomes gravity waves. The restoring force of gravity waves is gravity. Operating in the frequency band 3 MHz to 30 MHz, HF radar has operating wavelengths that are of the same order of magnitude as ocean surface gravity waves. Thus, HF radar signals interact strongly with the ocean gravity waves.

When the water depth is greater than approximately one-half of the ocean wavelength, deep water can be assumed. In deep water, the hydrodynamic dispersion relation of gravity waves may be expressed as (see, for example, Kinsman [26])

$$\omega = \sqrt{gK} , \quad (2.1)$$

where g is the acceleration due to gravity, ω is the radian frequency of an ocean wave and K is the corresponding ocean wavenumber. Ocean waves of wavenumber K and radian frequency ω will travel with a phase velocity, v_p , given by

$$v_p = \omega/K = \sqrt{g/K} . \quad (2.2)$$

Of course, these waves may travel in all directions, one of which will be in line with radar look direction and one of which will be opposite to radar look direction, and their

wavelengths are half of the radar wavelength. Therefore we can denote their speed v_p as

$$v_p = \omega/K = \pm\sqrt{g/K} = \pm\frac{1}{2}\sqrt{\frac{g\lambda}{\pi}}. \quad (2.3)$$

where the \pm indicates the advancing and receding directions, respectively, of the ocean waves with respect to the radar look direction.

Given that HF radars, for the purpose at hand, are deployed along the shoreline, for the case where there is a large distance from the radar to the ocean scattering patch, it is reasonable to assume that radio waves illuminate the ocean surface at grazing incidence. If λ is the wavelength of surface waves and λ_0 is the wavelength of radio waves, the Bragg scatter will occur when the

$$\lambda_0 = 2\lambda \sin \theta, \quad (2.4)$$

where θ is the angle of incidence (relative to the surface normal). For grazing incidence, $\theta = 90^\circ$ and thus the Bragg scatter condition becomes

$$\lambda_0 = 2\lambda. \quad (2.5)$$

where the water waves satisfying this relation are referred to as Bragg waves. This relation can be also expressed in term of the wavenumber, K , of the ocean wave and radio wave as

$$K = 2k_0. \quad (2.6)$$

Although a small amount of radar energy is scattered back to the radar receiver by each ocean-wave crest, for the case of the distance between adjacent ocean crests being exactly half the radar wavelength there will be a phase-coherent reinforcement of radar waves

reflected from the ocean surface. The coherent reflection greatly enhances the strength of the echo compared with all the other incoherent reflections from ocean waves with other wavelengths. This phenomenon is similar to the behavior of a diffraction grating.

The relative movement between the radio source and the ocean waves will cause Doppler shifts with respect to the radar carrier frequency in the radar return. The size of the shift is a function of the radar operating frequency. Furthermore, since the Bragg waves travel toward and away from the radar, this will correspond to two Doppler shifts in opposite directions from the radar carrier frequency. The large spectral peaks which may result from this so-called first-order Bragg interaction should, theoretically, appear at radian Doppler frequencies, ω_B , given by

$$\omega_B = \pm\sqrt{2gk_0}, \quad (2.7)$$

if there is no underlying current. Equivalently, if f_0 is the radar frequency in megahertz (MHz), the Bragg frequency f_B in hertz (Hz) may be easily shown to be

$$f_B = \pm 0.102\sqrt{f_0}, \quad (2.8)$$

which indicates a square-root dependence of the Doppler shift upon the radar operating frequency. This can be used to distinguish the Doppler shift imposed by an ordinary hard target, for which the Doppler shift depends linearly on the radar frequency.

In the bistatic model, the expression for ω_B is somewhat modified from the monostatic result given above. The geometry of the bistatic configuration is shown in Figure 2.1. The path directed from the transmitter (T) to the receiver (R_b) is the reference direction, which is denoted as the x -axis direction throughout this thesis. The line connecting the transmitter and bistatic receiver is defined as the baseline. T and R_b are foci of an elliptical scattering patch [13]. Scattering patch P is a position on this curve where the

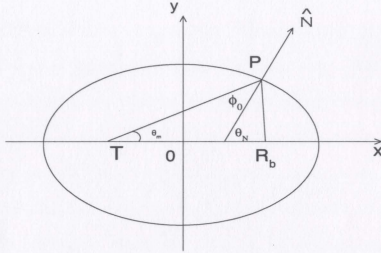


Figure 2.1: The general geometry of the bistatic configuration.

unit ellipse normal is \hat{N} . The angle θ_N from $\overline{TR_b}$ to the unit normal is precisely the direction of the Bragg scattering wave vector. The angle $\angle TPR_b$ is divided by the ellipse normal into two equal angles. Half of $\angle TPR_b$ is defined as the bistatic angle ϕ_0 . Still, assuming the deep water, the Doppler frequencies of the first-order peaks are [13]

$$\omega_B = \pm \sqrt{2gk_0 \cos \phi_0}. \quad (2.9)$$

Comparison of expressions (2.7) and (2.9) for the Bragg peak positions for monostatic and bistatic models, respectively, indicates the difference lies in the explicit appearance of the bistatic angle in (2.9). Clearly, when the bistatic angle ϕ_0 is equal to 0° , the bistatic model will be reduced to monostatic model. In this thesis, both bistatic and monostatic models will be employed. The bistatic first-order and second-order cross sections developed by Gill and Walsh [13] will be introduced, reproduced, and calculated in the following section. The monostatic model will be simply considered as a special case of the bistatic model when the bistatic angle is 0° .

In the radar return Doppler spectrum, there is usually a higher order continuum sur-

rounding the two significant first-order peaks (see Figure 2.2 of Section 2.2). This higher order continuum includes second-order scatter that may occur from a single reflection from second-order ocean waves, or from two scatters of first-order waves. There are nulls between the first- and second-order curves. Under the special conditions when the ocean wave direction is along or in the opposite direction to the radar beam for monostatic and to the ellipse normal for bistatic radar configurations, there will be only one first-order peak in the radar return Doppler spectrum, either in the negative or positive part. The higher order scatter beyond the second has little effect upon the surface current measurement. Therefore, only the first- and second-order scatters will be considered in this thesis.

2.2 Radial Current Measurements

Although ocean surface waves are not perfectly sinusoidal, but rather trochoidal in nature, they can be decomposed by Fourier's theorem. By means of Fourier's theorem, the ocean surface can be represented as the superposition of waves of different amplitudes, phases, frequencies, and directions of traveling. Therefore, when the HF radio waves are scattered at the ocean surface, one particular Fourier component of the ocean waves will satisfy the Bragg condition. Without an underlying current, the resulting spectral peaks should be at two symmetrical positions relative to the carrier. If the ocean waves are transported by an underlying current, these peaks will be shifted from these symmetrical positions. The amount of this displacement can be used to measure the radial current.

For a given radar frequency, the locations of the theoretical Bragg peaks can be predicted by equation (2.8) for the monostatic case. The actual peaks in a real Doppler spectrum may be located numerically. The difference value (i.e. the Doppler shift) between the measured and the theoretical values of the Bragg frequency may be obtained for each side of spectrum. Theoretically, the difference on each side of spectrum should

be equal; however, noise may cause a discrepancy between the two sides. When the wind blows directly away from or toward the radar look direction, one peak will generally be buried in, or barely visible above the noise floor. In this case only one-half of the Doppler spectrum is processed. From the frequency difference, Δf , the radial component V_r of ocean current velocity along the radar look direction can be derived as (see, for example [3])

$$V_r = 0.5\Delta f\lambda_0 . \quad (2.10)$$

Figure 2.2 depicts a typical Doppler spectrum of sea echo from which a radial surface current may be extracted based on shifts in the Bragg peaks. The theoretical position of the Bragg peaks is indicated by f_B (dash line). The measured positions of the Bragg peaks are indicated by f'_B in this figure. The whole spectrum is shifted in one direction due to an underlying current and the magnitude of this shift may be used to determine the radial current by means of equation (2.10).

2.3 Vector Current Derived from Monostatic Radar

Based on the number of the radar systems involved in the current measurement, we may categorize the basic radar deployments as either dual-site or single-site. A full radar system in this thesis is defined as a system that contains a transmitter and a receiver at the same or different locations— i.e. a full system may be operated monostatically or bistatically.

2.3.1 Single-site Approach

A single-site radar system can be used to obtain vector current [22, 27]. In this approach, the surface current vector is estimated from the radial currents based on the assumption

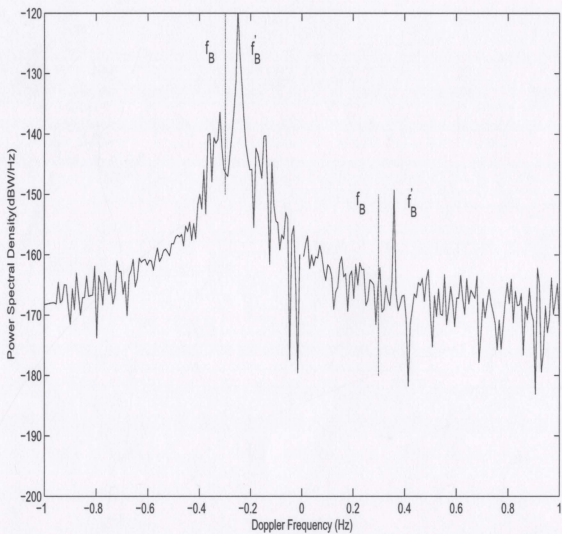


Figure 2.2: The simulated radar Doppler spectrum (power spectral density, PSD) with zero-mean stationary Gaussian noise. The radar operating frequency is 15 MHz, the bistatic angle is 55° , and the wind speed is 10 m/s, 75° to the x -axis.

of a uniform current distribution in the region of measurement. By definition, in this region, the spatial variability of the currents should be insignificant. The radial currents along several consecutive cells will simply be the projections of this uniform current along the different directions. Lipa [27] obtains the current vector by fitting the data in a least-squares method. Using a similar approach, Hickey [22] derived the vector currents and compared them with those obtained from drifter buoys in the same area. The positive results illustrate the potential of using single-site radar to extract the current maps. The main limitation of the signal-site method, however, is the assumption of uniform current distribution, since the surface currents are often observed to vary spatially and temporally.

2.3.2 Dual-site Approach

Dual-site radar systems consist of two spatially separated radars that survey a common coverage area. Radial currents can be obtained from each radar and, in the common coverage area, these can be combined through geometric manipulations to produce a vector current. However, the performance of the dual-site radar system is restricted by the limitation of the common coverage. Bobby [23] examines the ocean surface current by using two spatially separated radar facilities located in Cape Race and Cape Bonavista that cover a common ocean surface. The radial currents are derived from each set of radar data. The vector currents are produced using both Cartesian and cylindrical coordinate methods. The results of his research further validate the dual-site method and the potential for using the continuity equation to estimate vector currents.

2.4 Bistatic Configuration with Constant Bistatic Angle

In the dual-site approach, we actually want to obtain the radial currents along two different directions with a specified angular separation. If we add another receiver to a full radar system but keep the two receivers widely separated, we can have a combined configuration of radar systems, one receiver R_m operating in the monostatic mode, co-located with transmitter T, and another receiver R_b operating in bistatic mode. Thus, with a single transmitter, we can achieve results similar to those for the dual-site approach. Therefore, the combined monostatic/bistatic radar configuration model can be viewed as an extension of the dual-site model.

In the common bistatic configuration as shown in Figure 2.1, the transmitter (T) and receiver (R_b) are foci of an elliptical scattering patch. The coordinates are selected so as to make T and R_b lie on the x -axis, symmetrical about the origin. As noted in Section 2.1, P is an arbitrary scattering patch on the elliptical scattering patch and \hat{N} is the unit normal to the ellipse at P. Because the sum of the distances from T to P and P to R_b are constants for a given series of patches along one elliptical locus, the delay between transmitter and receiver is fixed for those patches. We may scan the ocean surface along the elliptical path of ellipse as described in [13]. However, along this path, the bistatic angles, and thus the positions of the first-order peaks in the Doppler spectra, change for different positions. This means that for one transmitted frequency, at the patches of different bistatic angles, we actually measure the radial currents added to ocean waves with different wavelengths. Furthermore, when we convert the two radial currents to a current vector, as will be seen, the angle of separation between the two radial currents plays an important role in the overall accuracy of the derived vector current. When the bistatic angle changes, the overall error in the current vector measurement will change

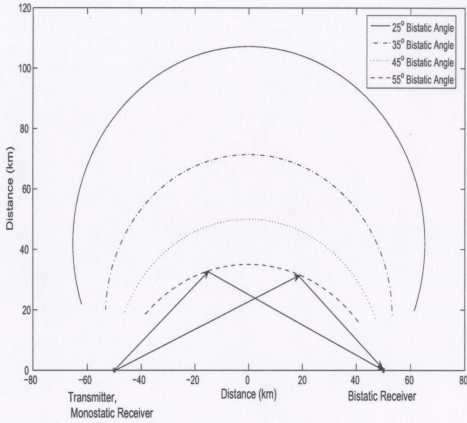


Figure 2.3: Locus of constant bistatic angle.

even if both radial currents having the same uncertainty.

From another perspective, to examine the Bragg wave with constant wavelength the bistatic angle should be kept constant. The scatter patch may move along a path as depicted in Figure 2.3. Four curves are plotted in this figure corresponding to 25°, 35°, 45°, and 55° bistatic angles, respectively. For a particular curve, for one operating frequency, the wavelengths of the Bragg waves sensed by the monostatic and bistatic receivers are different but the differences between them are fixed.

If the bistatic angle is assigned to be ϕ_0 , and θ_m is the monostatic “look” direction (see Figure 2.4), the bistatic “look” direction θ_N can be written as [13]

$$\theta_N = \theta_m + \phi_0 . \quad (2.11)$$

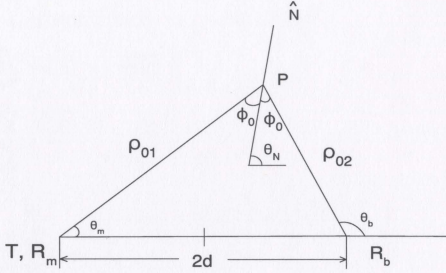


Figure 2.4: The geometric relationship of the bistatic and monostatic radar look directions with bistatic angle of ϕ_0 . T, R_m and R_b represent the transmitter and monostatic and bistatic receivers, respectively.

From Figure 2.4 the angle θ_b for bistatic receiver can obviously be expressed as

$$\theta_b = 2\phi_0 + \theta_m. \quad (2.12)$$

Also in the Figure 2.4, ρ_{01} is the distance between the transmitter and scatter patch, and ρ_{02} is the distance between the scatter patch and receiver. If the distance between T and R_b is $2d$, by trigonometric manipulation, we can express ρ_{01} and ρ_{02} in terms of ϕ_0 , θ_m , θ_R , and $2d$. There are four possibilities:

1. If $\phi_0 < \pi/4$, and θ_m , $\pi - \theta_b < \pi/2$, we have, from the law of sines

$$\rho_{01} = \frac{2d \sin \theta_b}{\sin 2\phi_0} \quad (2.13)$$

and

$$\rho_{02} = \frac{2d \sin \theta_m}{\sin 2\phi_0}. \quad (2.14)$$

2. If $\phi_0 < \pi/4$, $\theta_m < \pi/2$, but $\pi - \theta_b > \pi/2$, we have

$$\rho_{02} = \frac{2d \sin \theta_m}{\sin 2\phi_0} \quad (2.15)$$

and

$$\rho_{01} = \sqrt{\rho_{02}^2 + 4d^2 - 4d\rho_{02} \cos(\pi - \theta_b)}. \quad (2.16)$$

3. If $\phi_0 < \pi/4$, $\pi - \theta_b < \pi/2$, but $\theta_m > \pi/2$, we have

$$\rho_{01} = \frac{2d \sin \theta_b}{\sin 2\phi_0} \quad (2.17)$$

and

$$\rho_{02} = \sqrt{\rho_{01}^2 + 4d^2 - 4d\rho_{01} \cos \theta_m}. \quad (2.18)$$

4. Finally, if $\phi_0 > \pi/4$, and $\pi - \theta_b$, $\theta_m < \pi/2$, we have

$$\rho_{01} = \frac{2d \sin \theta_b}{\sin \theta_b \cos \theta_m - \sin \theta_m \cos \theta_b} \quad (2.19)$$

and

$$\rho_{02} = \sqrt{\rho_{01}^2 + 4d^2 - 4d\rho_{01} \cos \theta_m}. \quad (2.20)$$

In the Cartesian coordinate system where T and R_b are located symmetrically around the origin on x-axis, their coordinates are (-d, 0) and (d, 0), respectively, and the y-

component of the scatter patch can be written as

$$y = \rho_{01} \sin \theta_m . \quad (2.21)$$

For the x -coordinate, if $\rho_{01} > \rho_{02}$, we have

$$x = \rho_{01} \cos \theta_m - d , \quad (2.22)$$

and if $\rho_{01} < \rho_{02}$

$$x = -(d - \rho_{01} \cos \theta_m) . \quad (2.23)$$

There are two advantages to selecting the scattering patch along the constant bistatic angle. One advantage is that for this case, the bistatic receiver will always detect the radial current associated with ocean waves of a fixed wavelength. Another advantage lies in error prediction. Error exists in each radial component. When converting the radial current to vector current, the overall error depends on the angular separation between the two radial components, that is, on the bistatic angle. Assuming the radial currents are obtained with the same accuracy, different bistatic angles correspond to different accuracies in the vector current. This will be discussed in detail in Chapter 3.

The drawback of this configuration is that the delay between the transmitter and receiver is changing all the time. Care will have to be taken in extracting the time series from each receiver to exactly pick out a specific patch of interest.

2.5 From Radial Currents to Vector Current

At this stage, we consider two radial current components that are estimates of the projections of a vector current onto the radar look directions. In this section we will combine

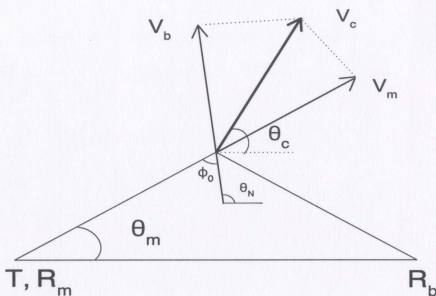


Figure 2.5: The current vector is obtained from the combination of the radial current components, V_m and V_b .

the two radial components by means of geometric manipulation to recover the vector current.

If V_c is denoted as the magnitude of the surface current and θ_c the direction of the current, two radial current components, V_m and V_b , are projections along the two radar look directions (ellipse normal direction for bistatic radar) as shown in Figure 2.5. They may be expressed as

$$V_m = V_c \cos(\theta_c - \theta_m) \quad (2.24)$$

and

$$V_b = V_c \cos(\theta_c - \theta_N), \quad (2.25)$$

where V_m is the radial current along the monostatic look direction θ_m and V_b is that along the bistatic look direction θ_N . Since V_m and V_b are pointed in different directions, there is an intersection between them that is actually equal to bistatic angle ϕ_0 in our

configuration. If V_m and V_b are known, solving the above equations will produce the vector current direction with respect to the x -axis as

$$\theta_c = \tan^{-1} \left(\frac{V_b \cos \theta_m - V_m \cos \theta_N}{V_m \sin \theta_N - V_b \sin \theta_m} \right) \quad (2.26)$$

and the current magnitude as

$$V_c = \frac{V_b}{\cos(\theta_c - \theta_N)}. \quad (2.27)$$

It may be observed from the above equations that when the bistatic angle ϕ_0 is very small — i.e. close to 0° — or very large — i.e. close to 90° — which means two sets of radial currents lie nearly parallel to each other, the vector current cannot be robustly produced. The reason why this is the case is that, as we note from equation (2.26), the calculated θ_c will be perpendicular or anti-perpendicular to θ_N . Then, from equation (2.27), large fluctuations in magnitude V_c will appear. This is the so-called baseline instability. The baseline instability can be also defined from the x and y components in the Cartesian coordinate system [22]. We will further discuss the baseline instability and other errors in Chapter 3.

Chapter 3

Error Analysis

As noted in the previous chapter, the approach to extract the vector current from HF surface wave radar data includes two steps: (1) obtaining the radial currents from the first-order peaks of the radar receiver signal and (2) combining the radial currents to produce the vector current. Errors that occur in both steps will be analyzed and discussed in this chapter.

3.1 Errors in Radial Current Measurements

When we address the errors in this section, we assume that all the radar data with signal to noise ratio (SNR) below the threshold, typically around 25 dB, have been discarded. Generally, there are two groups of errors: systematic error and statistical error. The sources of systematic error include antenna pattern distortions, which are system-dependent and even site-dependent, distortions from ships or other large objects visible by radar and other distortions from shallow water or third-order wave-wave interaction [28]. Sources of statistical errors include atmospheric noise, ionospheric echo, man-made noise, and random current variation over the patch of ocean. Statistical errors can be mitigated by proper averaging. The averaging may be done spatially or temporally or

both.

When Doppler spectra are estimated in this work, the periodogram method is used — i.e., the spectra are simply an average of the squared FFT's of segments of the data time series. If it is assumed that the radar data are of high quality and that there is no spatial variation of currents within a range cell, the resolution of the FFT can be used to characterize the error in the radial current values. The FFT resolution is an important parameter that indicates the radar's ability to distinguish one frequency component from its neighbors. In the periodogram method, the resolution of measurement is defined as the reciprocal of time interval for the FFT calculation.

It is known that the error of the FFT has a uniform distribution between two adjacent frequencies. In order to have better FFT resolution, the time interval for the FFT calculation should be chosen longer. This implies that over the measuring time interval the ocean current condition should be stationary. For the simulation and analysis throughout this thesis, 4096-point time series will be used and the sampling interval is set to be 0.25 s, corresponding to a nearly 20-minute time interval. This time interval has been used for the measurement of wind driven surface current [20]. Under this simulation condition the FFT resolution is fixed as 0.0078 Hz for the Doppler spectra in the monostatic and bistatic radar look directions. By applying equation (2.10), the radial current resolution in speed, Δv_r , can be found. For the operating frequencies of 6.75 MHz, 15 MHz, and 25 MHz, the monostatic receiver has the radial current resolutions of ± 8 cm/s, ± 4 cm/s, and ± 2.3 cm/s, respectively. For the bistatic radar look direction, however, the resolution will be coarser than the monostatic side and be a function of the bistatic angle ϕ_0 . This can also be calculated by means of equation (2.10) with a modified radar operating wavelength $\lambda'_0 = \frac{\lambda_0}{\cos \phi_0}$, i.e.

$$V_r = 0.5 \Delta f \lambda'_0. \quad (3.1)$$

3.2 Errors in Vector Current Combination

The accuracy of vector current largely depends on the intersection angle between the two radar look directions if the same random errors are assumed for the two radial current components. If there were no error terms in either of the radial currents, the vector current could be perfectly obtained by equations (2.26) and (2.27), no matter how small the intersection angle. However, in this simulation randomness is added and the error will be present in the radial current measurements for both radial directions. As a result, the intersection angle will play an important role in the extraction of the total vector current. Geometric dilution of precision (GDOP) is a unitless coefficient that can be used to quantitatively describe the uncertainties in current vector combination due to geometry.

GDOP was first introduced in the Global Positioning System (GPS) navigation system. Its sole purpose is to predict the purely geometric influence and does not take into account any other effects that might be expected to influence the accuracy of the measurement. Chapman *et al.* [29] borrowed this concept for ocean current measurement involving a pair of HF backscatter radars. An expression of GDOP was derived in term of the radar mean look direction and the intersection angle between the two radar beams. In this thesis, the same expression of the GDOP will be developed but in a more straightforward way. The idea of GDOP could be helpful in analyzing the error of vector current measurement when one of the radial current components is extracted by means of the bistatic radar receiver.

Mathematically, the current vector can always be decomposed into two orthogonal components, u and v . In Figure 3.1, V_1 and V_2 are the radial currents measured along two arbitrary radar look directions, α and β are the angles from the x -axis to the two radar look directions, respectively, and the intersection angle between these two radar

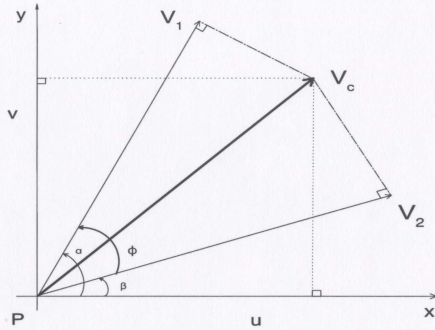


Figure 3.1: Geometrical relation of the current components.

look directions is ϕ . Thus, we have

$$\begin{aligned} V_1 &= u \cos \alpha + v \sin \alpha \\ V_2 &= u \cos \beta + v \sin \beta . \end{aligned} \quad (3.2)$$

These equations are solved for u and v , as

$$\begin{aligned} u &= \frac{V_1 \cos \beta - V_2 \cos \alpha}{\sin \alpha \cos \beta - \cos \alpha \sin \beta} \\ v &= \frac{V_1 \sin \beta - V_2 \sin \alpha}{\sin \alpha \cos \beta - \cos \alpha \sin \beta} . \end{aligned} \quad (3.3)$$

The denominators of these two equations are identical and

$$\sin \alpha \cos \beta - \cos \alpha \sin \beta = \sin(\alpha - \beta) = \sin \phi , \quad (3.4)$$

which gives

$$\begin{aligned} u &= \frac{V_1 \cos \beta - V_2 \cos \alpha}{\sin \phi} \\ v &= \frac{V_1 \sin \beta - V_2 \sin \alpha}{\sin \phi}. \end{aligned} \quad (3.5)$$

The error associated with radial currents V_1 and V_2 are assumed to be uncorrelated and their standard deviations are defined as σ_1 and σ_2 , respectively. Therefore, the standard deviations with respect to u and v can be written as [30]

$$\begin{aligned} \sigma_u^2 &= \frac{\sin^2 \beta + \sin^2 \alpha}{\sin^2 \phi} \sigma_1^2 \\ \sigma_v^2 &= \frac{\cos^2 \beta + \cos^2 \alpha}{\sin^2 \phi} \sigma_2^2. \end{aligned} \quad (3.6)$$

The GDOP is defined as [31]

$$\text{GDOP} = \sqrt{\frac{\sigma_u^2}{\sigma_1^2} + \frac{\sigma_v^2}{\sigma_2^2}}. \quad (3.7)$$

Equation (3.7) shows that the GDOP is always positive, and only related to the directions of the two radial components and the intersection angle between them. If we further assume that the standard deviations of the errors in both radar look directions are identical, i.e. $\sigma_1 = \sigma_2 = \sigma$, we have

$$\text{GDOP} = \frac{\sqrt{2}}{|\sin(\phi)|}, \quad (3.8)$$

which means that the GDOP is only a function of the intersection angle between the two radar look directions. Figure 3.2 depicts an example of the GDOP described by equation (3.8) with the intersection angle changing from 0° to 180° . It is observed that the lowest GDOP appears when the intersection angle is 90° . If the intersection angle changes from

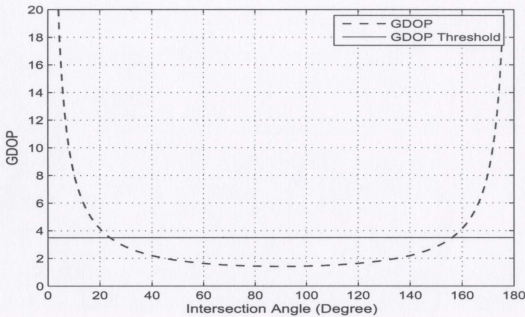


Figure 3.2: The plot of GDOP against the intersection angle (dashed line). The solid line indicates a threshold of GDOP as an example. The GDOP values that exceeds the threshold will be discarded.

0° to 90° , the GDOP will decrease and result in decreasing error of combination. On the other hand, as the intersection angle changes from 90° to 180° , the GDOP will increase and result in increasing error of combination. GDOP values will be used as a threshold in vector current combination. For geometrical relationships with lower GDOP values, the errors in the vector currents will also be lower.

In Figure 2.1, when the measured region approaches to the baseline of the radar configuration, the intersection angle will approach to 180° and the corresponding GDOP will become infinite from equation (3.8). This is denoted as the baseline instability indicated in Section 2.5, since no reliable vector current will be obtained. Another extreme case is when the scattering region is far away from the baseline of the radar system, the intersection angle will approach to 0° . In this situation, we still cannot get reliable vector currents because of higher GDOP value (equation (3.8)). We may call this the far-zone instability and it is similar in effect to the baseline instability. Both baseline and far-zone instabilities cannot be completely removed. However, they may be limited to a negligible

level by choosing moderate GDOP threshold values. Figure 3.2 shows a GDOP threshold value of 3.5, corresponding to the intersection angles that are 25° and 155° , respectively. Those angles that are less than 25° or greater than 155° will cause a rapidly increasing GDOP and result in significant unreliability in current combination. Equation (3.8) has been used in the selection of reliable range cells for HF radar vector current measurement [20, 29].

The previous discussion of GDOP is concerned with a two-radar current measurement system in which each radar operates monostatically. We can borrow the idea of GDOP for HF radar current measurement when one of the radar receivers is in the bistatic configuration. Under this radar configuration, the bistatic Bragg frequency is a Doppler frequency shift due to a moving object along the direction of \hat{N} , which will be denoted as the bistatic radar look direction, and the intersection angle defined previously will be equal to the bistatic angle ϕ_0 (Figure 2.1). The most significant difference that needs to be explored further is that the uncertainty of the radial current component along the bistatic radar receiver is a function of the bistatic angle. The assumption of identical deviations, $\sigma_1 = \sigma_2 = \sigma$, cannot be invoked in equation (3.7) to reach equation (3.8). However, since all the current measurements are based on simulated data in this work, a known current vector can be selected as the ground truth and the uncertainty of the current combination can be investigated numerically. Specifically, if the errors in both radial components are assumed within FFT resolution and their distributions are uniform, it is possible to predict the maximum errors of vector current both in magnitude and direction. An example is depicted in Figure 3.3 to show the maximum errors in magnitude and direction when the bistatic angle changes from 0° and 90° . In Figure 3.3, the errors in the currents in both radial components are different but fixed in magnitude when the bistatic angle varies. In fact, when the bistatic angle increases, the bistatic Bragg frequency f_B (Figure 2.2) will decrease accordingly and the wavelength of the corresponding Bragg wave will

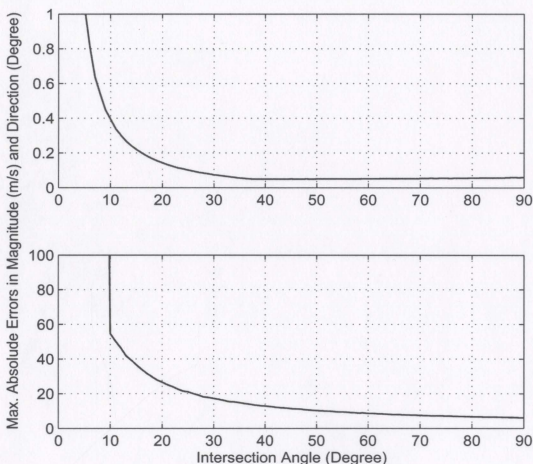


Figure 3.3: The maximum errors in magnitude and direction when the bistatic angle changes from 0° and 90° . The input current is 0.6 m/s, 60° to the x -axis. The errors in monostatic and bistatic radar look directions are 4.5 cm/s and 5 cm/s, respectively.

increase. Therefore, the radial current resolution in the bistatic radar direction will be a function of the bistatic angle. Under this consideration, the errors in magnitude and direction of the vector current combination are investigated numerically from different aspects. The results are shown in Figures 3.4 to 3.7 for discussion.

In Figure 3.4 a vector current of 0.6 m/s, 60° to the x -axis is measured by an HF radar system with monostatic and bistatic receivers. The maximum combination errors in magnitude and direction are depicted as a function of the intersection angle (bistatic angle). The FFT resolution is fixed as 0.0078 MHz. Three radar operating frequencies, 6.75 MHz, 15 MHz, and 25 MHz are checked, corresponding to the radial current errors of

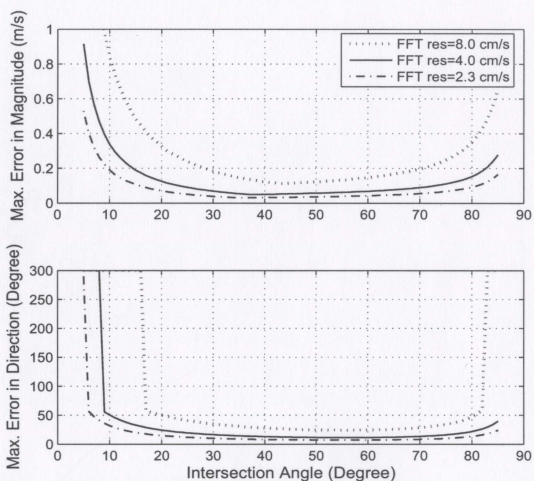


Figure 3.4: The maximum errors in magnitude and direction as a function of the intersection angle (bistatic angle) when a vector current is measured by an HF radar system with monostatic and bistatic receivers. The current is 0.6 m/s, 60° to the x -axis.

± 8.0 cm/s, ± 4.0 cm/s, and ± 2.3 cm/s, respectively, along the monostatic radar direction equation (2.10). However, in the bistatic radar look direction the radial current error will not be a fixed value for each radar frequency and should be calculated by equation (3.1). It is observed in Figure 3.4, that the combination errors in both magnitude and direction increase quickly when the bistatic angles are below 25° or beyond 75° . This result is very similar to the plot of GDOP against the intersection angles in Figure 3.2. The reason why the errors of vector current increase significantly below 25° or beyond 75° is that the FFT error in the bistatic direction is close to or beyond the radial current speed itself. This result implies that it is necessary to set a pair of thresholds in the bistatic angles to

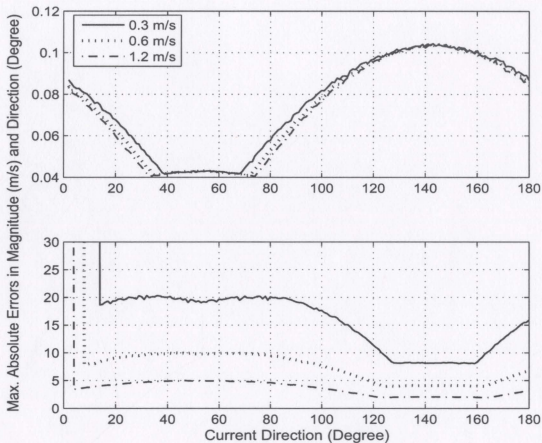


Figure 3.5: The maximum errors of the current magnitude and direction when two radar receiver beams are 30° and 75° to the x -axis (the bistatic angle is 45°). The magnitudes of currents are 0.3 m/s, 0.6 m/s, and 1.2 m/s, respectively. The FFT resolutions in both directions are 4 cm/s.

calculate the vector current. In future simulation the bistatic angles between 25° to 75° are chosen as the applicable bistatic angles.

In another test, the look directions of the two radars are fixed and the magnitude of the current is also fixed, while the direction of current changes from 0° to 180° . For the fixed FFT resolution, the accuracy of the retrieved vector current still varies with the relative positions between the two radar directions and current direction, although this variation is not very significant. Figures 3.5 and 3.6 show the maximum errors in magnitude and direction. In Figure 3.5, the FFT resolutions on both radial components are the same. In Figure 3.6, the FFT resolutions on the two radial components are 4 cm and 6 cm, respectively.

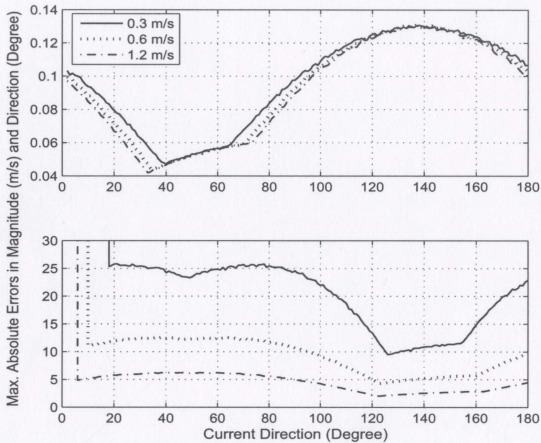


Figure 3.6: The same as Figure 3.5, except the FFT resolutions in two directions are 4 cm/s and 6 cm/s, respectively.

The curves in Figures 3.5 and 3.6 correspond to the maximum variation ranges of the direction and magnitude. It can be seen that when the current direction is located between the two radar look directions, the variation of magnitude is relatively small but the variation of direction is large, and *vice versa*.

Figure 3.7 is a more comprehensive example. In this figure, a set of vector currents with speed 0.8 m/s and different directions are measured. The angular separations between the two radar look directions are the same as in Figure 3.5. The arrows indicate vector currents and various directions of 10°, 40°, 70°, 100°, and 130°, respectively. Radial current resolution in radar look direction 1 is set to be 4 cm/s and in radar look direction 2 is set to be 6 cm/s. Each parallelogram represents the range of the measured vector current. These parallelograms are defined by the bistatic angles and resolutions on both

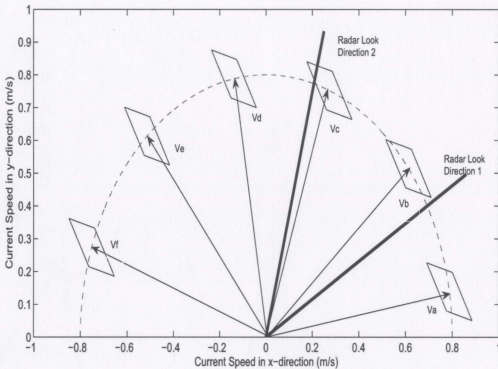


Figure 3.7: The prediction of changing range. A set of vector currents are with speeds 0.8 m/s, and in the directions of 10° , 40° , 70° , 100° , and 130° , respectively. The two radar look directions are 30° and 75° . All angles are with respect to x -axis.

sides of radar look directions. The diagonals of the parallelograms are generally different in length. When the measured current is between two radar look directions, such as Vb and Vc , the variation in magnitude is determined by the shorter diagonal, whereas the variation in direction is determined by the longer diagonal. These indicate that the variation in the magnitude measurement is less than in the direction measurement. However, when the current directions are outside the radar look directions, such as Va , Vd , Ve , and Vf , the variation of magnitude is determined by the longer diagonal and variation of direction is determined by the shorter one, corresponding to a better measurement in current direction and worse measurement in magnitude. It is also observed that the magnitude of the input current has less influence on the accuracy in the measurement of current magnitude than it does on the accuracy in the measurement of direction.

Chapter 4

Vector Current Extraction from Simulated Bistatic Data

Since the majority of the experiments of HF radar ocean surface current measurements are based on the monostatic configuration, the bistatic radar data have to be simulated first for further investigation. The HF radar data used in this research are simulated based upon the first- and second-order bistatic cross sections of the ocean surface developed by Gill and Walsh [13]. In this chapter, we first introduce the models for the bistatic cross sections and from these obtain the power spectral density (PSD) of the ocean echo. Time series of the radar received signals will be simulated by means of the method of inverse transformation from the PSD of the Doppler radar spectrum, and the ocean current information and noise will be added when this transformation is accomplished. Then Doppler spectra are estimated by the periodogram method and finally radial currents are extracted.

4.1 Review of Cross Sections

As noted in Chapter 2, the underlying physical mechanism, first conjectured by Crombie [25], that accounts for the peaks in HF Doppler radar spectra is Bragg scattering. As seen already, in a typical spectrum there are two well-defined peaks, which are denoted as first-order or Bragg peaks and these peaks are surrounded by a higher order continuum. In the absence of surface currents, the positions of the first-order peaks are symmetrical about the radar carrier frequency and are proportional to the square root of the radar operating wavenumber k_0 .

HF radar cross sections of the ocean surface which form the basis of HF technology is the focus of this section and will be used throughout this research. In the following sections, the bistatic first-order and second-order cross sections of Gill and Walsh [13] are reviewed. The chief purpose for considering the second-order cross section is that it is useful when determining the width of the first-order peaks — i.e. it is important to observe the nulls between the first- and second-order components. In the second-order cross sections, only the patch scattering term will be considered. Other cross section components found in [13] that have little influence on the current measurement will not be a topic in this research.

4.1.1 Directional Ocean Wave Spectra

Any description of the scattering of the radar signal from the ocean surface obviously must incorporate a model of that surface. This model will be addressed in advance, following the description of Gill [15].

Typically, the ocean spectrum of wavenumber K , $S_1(\vec{K})$, whose dominate direction in $\theta_{\vec{K}}$ may be expressed as the product of a non-directional spectrum, $S_1(K)$, and a

normalized directional factor, $g(\theta_{\vec{K}})$ [32]:

$$S_1(\vec{K}) = S_1(K)g(\theta_{\vec{K}}) . \quad (4.1)$$

The normalization on $g(\theta_{\vec{K}})$ is such that

$$\int_0^{2\pi} g(\theta_{\vec{K}}) d\theta_{\vec{K}} = 1 . \quad (4.2)$$

Clearly,

$$\int_0^{2\pi} S_1(\vec{K}) d\theta_{\vec{K}} = S_1(K) . \quad (4.3)$$

The Pierson-Moskowitz non-directional spectrum S_{PM} [33] is selected as the ocean wave spectrum with a modification of

$$S_1(K) = \frac{1}{2} S_{PM}(K) \quad (4.4)$$

by Gill [15], where

$$S_{PM}(K) = \frac{\alpha_{PM}}{2K^4} \exp\left(\frac{-0.74g^2}{K^2 u_w^4}\right) . \quad (4.5)$$

In this equation, α_{PM} is a constant with value 0.0081 and u_w represents the wind speed measured at 19.5 m above the ocean surface.

The directional distribution $g(\theta_{\vec{K}})$ in equation (4.1) is actually also a function of wavenumber K , which can be written as

$$g(\theta_{\vec{K}}, K) = F(s(K)) \cos^{2(s(K))} \left[\frac{\theta_{\vec{K}} - \bar{\theta}(K)}{2} \right] , \quad (4.6)$$

where $s(K)$ is called the spread function and $\bar{\theta}(K)$ is the dominant direction of the waves [34]. In simulation, this $\bar{\theta}(K)$ is usually replaced by θ_w , the wind direction with respect to the radar look direction. When removing the dependence of frequency from the spread function [34], the simplified directional distribution is written as,

$$g(\theta_{\vec{K}}) = F(s) \cos^{2s} \left[\frac{\theta_{\vec{K}} - \theta_w}{2} \right]. \quad (4.7)$$

In our simulation, a typical value of $s = 2$ is chosen as has been suggested by previous investigators (for example, [15, 35, 36]). For this case,

$$F(s = 2) = \frac{4}{3\pi}. \quad (4.8)$$

Therefore, the directional ocean wave spectrum is obtained as

$$S_1(m\vec{K}) = \left[\frac{\alpha_{\text{PM}}}{4K^4} \exp \left(\frac{-0.74g^2}{K^2 u_w^4} \right) \right] \left[\frac{4}{3\pi} \cos^4 \left(\frac{\theta_{\vec{K}} + \frac{(1-m)\pi}{2} - \theta_w}{2} \right) \right]. \quad (4.9)$$

where the reference direction of θ_w is switched to the x -axis by means of a parameter $\frac{(1-m)\pi}{2}$ with $m = \pm 1$. With specific values of wind velocity, radar frequency, and bistatic angle, using the ocean wave model stated in equation (4.9), the first- and second-order radar cross sections can be computed. All the simulations carried out in this thesis are based upon this ocean wave model.

Figure 4.1 is an illustration of the Pierson-Moskowitz ocean-wave spectra as a function of wind speed and ocean wavenumber. Wind speeds are chosen to be 10 m/s, 13 m/s, and 16 m/s, respectively. It is noticed that the peak increases in amplitude and shifts to lower frequency as the wind speed increases. This has a significant effect on HF radar spectra, but does not affect the first-order cross section to any great extent. This is due to the fact that the ocean waves that produce the first-order peaks are general in the

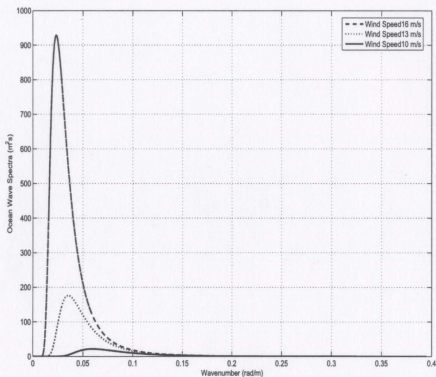


Figure 4.1: Pierson-Moskowitz ocean wave spectra as functions of wind speed and wavenumber.

high frequency end of the ocean spectrum, corresponding to the saturated region.

4.1.2 First-order Cross Section

For bistatic scattering, the Bragg frequencies are functions of the bistatic angle ϕ_0 and radio wavenumber k_0 . The expression for the first-order cross section $\sigma_1(\omega)$ is given as

[13]

$$\sigma_1(\omega) = 2^4 \pi k_0^2 \sum_{m=\pm 1} S_1(m\vec{K}) \frac{K^{\frac{5}{2}} \cos \phi_0}{\sqrt{g}} \Delta \rho_s S a^2 \left[\frac{\Delta \rho_s}{2} \left(\frac{K}{\cos \phi_0} - 2k_0 \right) \right]. \quad (4.10)$$

In this equation, ω is the radian Doppler frequency, $S_1(m\vec{K})$ is the ocean directional wave spectrum with the scattering wave vector \vec{K} as stated in Subsection 4.1.1, and $\Delta \rho_s$ is the width of scattering patch, which is the smallest radial distance that can be unambiguously distinguished by the HF radar. Of course, $\Delta \rho_s$ depends on the pulse

width of the transmitted radar signal and is given by

$$\Delta\rho_s = \frac{c\tau_0}{2}, \quad (4.11)$$

where c is the vacuum speed of light (3×10^8 m/s) and τ_0 is the pulse width of the transmitted signal. The $m = \pm 1$ in equation (4.10) is used to distinguish the positive and negative portions of the Doppler shift, which arise from two sets of ocean waves, one moving along the direction of the ellipse normal and one moving in the opposite direction; i.e.

$$m = 1 \quad \text{when } \omega < 0 \quad (4.12)$$

and

$$m = -1 \quad \text{when } \omega > 0. \quad (4.13)$$

This is illustrated in Figure 4.2. Hence, the equation of the Doppler frequencies which are related to the scattering wavenumbers K by the dispersion relation is given by

$$\omega = -m\sqrt{gK}. \quad (4.14)$$

In the equation (4.10), it may be noted that it is a squared sampling function that generates the first-order peaks, while in Barrick's first-order cross section expression [6], it is a delta function corresponding to a plane wave transmitting waveform. In order to determine the Bragg wave scattering vector, the squared sampling function in the first-order cross section must be considered. This function is maximum when its argument is

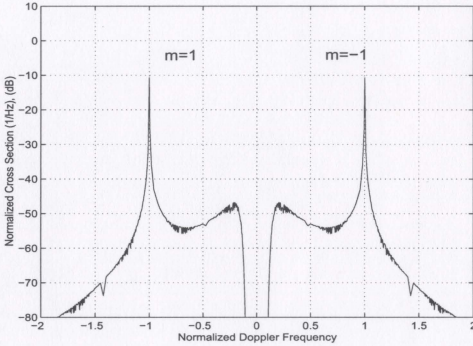


Figure 4.2: The two sections of the bistatic first-order cross section with $(m = \pm 1)$ indicates the positive and negative Doppler portions. The bistatic angle is 30° . The wind velocity is 15 m/s, perpendicular to the radar look direction.

zero; i.e. when

$$K = K_{Bbi} = 2k_0 \cos \phi_0 . \quad (4.15)$$

The wavenumber K_{Bbi} is associated with the Bragg peaks for bistatic scattering which is clearly a function of bistatic angle ϕ_0 . When $\phi_0 = 0$,

$$K_{Bmono} = 2k_0 , \quad (4.16)$$

in which the wavenumber K_{Bmono} is associated with the Bragg peaks for the monostatic case.

The first-order cross section can be computed directly from equation (4.10). As noted, Figure 4.2 shows an example of the first-order cross section for a bistatic angle of 30° and a wind velocity of 15 m/s, perpendicular to the radar look direction.

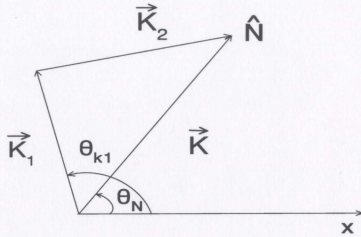


Figure 4.3: An enlarged view of the second-order scattering relations for the bistatic patch scattering.

4.1.3 Second-order Cross Section

The second-order patch scatter consists of two types of second-order interaction mechanisms between radar signal and water waves, one is due to the e-m signal interacting with a second-order ocean wave, another is from interaction between radar wave and two first-order ocean waves. If \vec{K}_1 and \vec{K}_2 are the wave vectors of the ocean waves, in order to generate the second-order bistatic scatter, \vec{K}_1 and \vec{K}_2 must satisfy the condition [13], as shown in Figure 4.3,

$$\vec{K}_1 + \vec{K}_2 = \vec{K} . \quad (4.17)$$

Here \vec{K} is in the direction of the ellipse normal θ_N (see Figure 2.1) and has a magnitude of $2k_0 \cos \phi_0$. Imposing the law of cosines, the magnitude of \vec{K}_2 may be obtained from

$$\begin{aligned} K_2^2 &= K_1^2 + K^2 - 2K_1K \cos(\theta_{\vec{K}_1} - \theta_N) \\ &= K_1^2 + 4k_0^2 \cos^2 \phi_0 - 4K_1k_0 \cos \phi_0 \cos(\theta_{\vec{K}_1} - \theta_N) , \end{aligned} \quad (4.18)$$

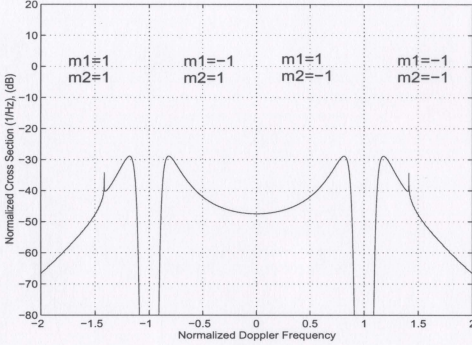


Figure 4.4: The four sections of the bistatic second-order cross section. The radar operating frequency is 25 MHz, the bistatic angle is 30° , the wind velocity is 15 m/s perpendicular to the radar look direction. Only the $K_1 < K_2$ case is simulated here.

where $\theta_{\vec{K}_1}$ is the angle of \vec{K}_1 from the x -axis. Then, the second-order cross section for patch scatter may be given as [13]

$$\begin{aligned}
 \sigma_{2P}(\omega_d) = & 2^3 \pi k_0^2 \Delta \rho_s \sum_{m_1=\pm 1} \sum_{m_2=\pm 1} \int_0^\infty \int_{-\pi}^\pi \int_0^\infty \{S_1(m_1 \vec{K}_1) S_1(m_2 \vec{K}_2) \\
 & \cdot |S \Gamma_P|^2 K^2 \cos \phi_0 \text{Sa}^2 \left[\frac{\Delta \rho_s}{2} \left(\frac{K}{\cos \phi_0} - 2k_0 \right) \right] \\
 & \delta \left(\omega_d + m_1 \sqrt{gK_1} + m_2 \sqrt{gK_2} \right) K_1 \} dK_1 d\theta_{\vec{K}_1} dK, \quad (4.19)
 \end{aligned}$$

in which $\delta(\cdot)$ is the usual Dirac delta function and the remaining parameters will be specified in the following paragraphs. Figure 4.4 is a typical example of a second-order bistatic cross section. As shown in the figure, there are four parts corresponding to four possible combinations of m_1 and m_2 , which represent four different Doppler frequency

regions in the second-order cross section, respectively. If $m_1 = m_2$,

$$\left. \begin{aligned} \omega < -\omega_B, \quad \text{when } m_1 = m_2 = 1 \\ \omega > \omega_B, \quad \text{when } m_1 = m_2 = -1 \end{aligned} \right\}. \quad (4.20)$$

If $m_1 \neq m_2$, $-\omega_B < \omega < \omega_B$, and

$$\left. \begin{aligned} -\omega_B < \omega < 0, \quad \begin{aligned} m_1 = -1, m_2 = +1 \text{ if } K_1 < K_2 \text{ or} \\ m_1 = +1, m_2 = -1 \text{ if } K_1 > K_2 \end{aligned} \\ \text{and} \\ 0 < \omega < \omega_B, \quad \begin{aligned} m_1 = -1, m_2 = +1 \text{ if } K_1 > K_2 \text{ or} \\ m_1 = +1, m_2 = -1 \text{ if } K_1 < K_2 \end{aligned} \end{aligned} \right\}. \quad (4.21)$$

In equation (4.19), the parameter ${}_S\Gamma_P$ is referred to as the coupling coefficient. It is defined as

$${}_S\Gamma_P = \frac{1}{2} \left[\Gamma_P(\vec{K}_1, \vec{K}_2) + \Gamma_P(\vec{K}_2, \vec{K}_1) \right]. \quad (4.22)$$

Here

$$\Gamma_P = {}_H\Gamma_P + {}_E\Gamma_P, \quad (4.23)$$

where ${}_H\Gamma_P$ is the hydrodynamic coupling coefficient and ${}_E\Gamma_P$ is the electromagnetic coupling coefficient. The hydrodynamic and electromagnetic coupling coefficients correspond to two mechanisms for the second-order interactions between ocean surface waves and electromagnetic waves. For the purpose of this work, the electromagnetic coupling coefficient does not affect the results [13] and will be neglected in the simulation. This non-critical omission also significantly affects the speed of the algorithm.

To calculate the second-order cross section, the squared sampling function of equation

(4.19) must be addressed. Gill and Walsh [13] show that for typical scattering patch widths it is possible to reduce that function to a delta function with the result being written as

$$\sigma_{2P}(\omega_d) \approx 2^6 \pi^2 k_0^4 \cos^4 \phi_0 \sum_{m_1=\pm 1} \sum_{m_2=\pm 1} \int_{-\pi}^{\pi} \int_0^{\infty} \left\{ S_1(m_1 \vec{K}_1) S_1(m_2 \vec{K}_2) \cdot |S \Gamma_P|^2 \delta \left(\omega_d + m_1 \sqrt{g K_1} + m_2 \sqrt{g K_2} \right) K_1 \right\} dK_1 d\theta_{\vec{K}_1}. \quad (4.24)$$

Then, the remaining delta function constraint in the second-order cross section equation (4.24) may be solved numerically [15].

4.1.4 Simulation of Cross Sections

HF radar bistatic cross section of the ocean surface are simulated and plotted for different radar frequencies, wind velocities, and bistatic angles in this subsection. The behaviors of cross sections for the different parameters will be briefly discussed.

1. The Effects of Wind Directions

Figure 4.5 portrays the bistatic cross sections with different wind directions $\theta_w = 0^\circ, 45^\circ, 90^\circ, \text{ and } 135^\circ$ relative to x -axis, respectively, at the same wind speed of 15 m/s. The bistatic angle is $\phi_0 = 45^\circ$ (see Figure 2.4) and the radar operation frequency is $f_0 = 15$ MHz. It can be seen that the relative strengths of the left and right Bragg peaks are highly related to wind direction. When the wind direction is perpendicular to the ellipse normal direction (bistatic look direction) in bistatic model (see Figure 4.5a), the energy carried by the two Bragg peaks is similar. When the wind direction is parallel or antiparallel to the ellipse normal direction, one side of the peaks will be greatly enhanced (see Figure 4.5c). When the wind directions are symmetrical with respect to the ellipse normal, as in the case for $\theta_w = 45^\circ$ or 135° , the two cross section plots are essentially identical (see Figures 4.5b and 4.5d).

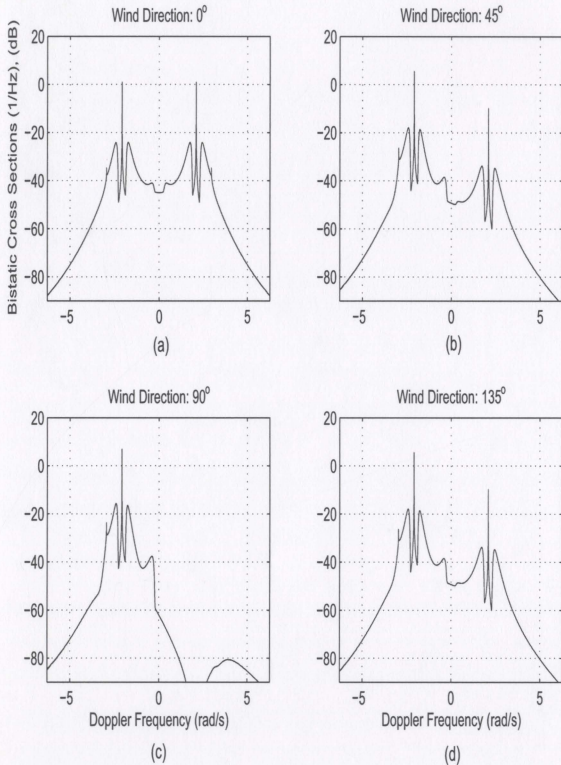


Figure 4.5: Bistatic cross sections for a wind speed of 15 m/s with different wind directions of $\theta_w = 0^\circ$, 45° , 90° , and 135° , respectively. The bistatic angle $\phi_0 = 45^\circ$ (see Figure 2.4) and the radar operation frequency $f_0 = 15$ MHz.

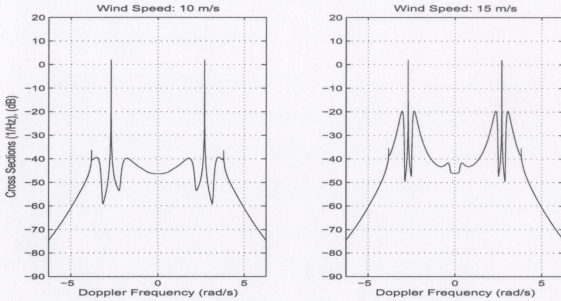


Figure 4.6: Bistatic cross sections for wind speeds of 10 m/s (left) and 15 m/s (right) with wind direction 0° to x -axis. The radar operating frequency is 15 MHz and the bistatic angle is 45° .

Similar results will occur for a monostatic configuration where the ellipse normal is replaced by the narrow beam look direction. From the property described above, theoretically speaking, wind direction is one of the ocean surface parameters that can be detected by HF radar, and some research has been focused on this topic (see for example, [37–39]).

2. The Effects of Wind Speed

The ocean wave spectrum is a function of wind speed as defined in equation (4.9). Since both the first- and second-order radar cross sections are functions of the ocean wave spectrum, wind speed will affect the radar cross section. Figure 4.6 illustrates this by changing the wind speed while keeping the radar frequency, bistatic angle, and wind direction fixed. Here, the wind speeds are selected as $u_w = 10$ m/s and 15 m/s, respectively and the same wind direction $\theta_w = 0^\circ$ is assumed. The radar operating frequency is 15 MHz and the bistatic angle is 45° . It is observed that the magnitude of the second-order cross section will increase significantly with the increasing of wind speed.

3. The Effects of Radar Frequency

The bistatic first- and second-order cross sections for radar operating frequencies of 25 MHz, 15 MHz, and 6.75 MHz are depicted in Figure 4.7. The same wind speed $u_w = 10$ m/s, wind direction $\theta_w = 0^\circ$, and bistatic angle $\phi_0 = 45^\circ$ are used to obtain these cross sections. Clearly, the Doppler shifts of the first-order peaks are altered corresponding to the radar frequencies. The behavior of the second-order cross section in the regions near the Bragg peaks is significantly different between the higher and lower radar operating frequencies. When the radar frequency is at 25 MHz, the continuum adjacent to the Bragg peaks is clear and quite distinct, which indicates that the majority of the ocean spectral energy is mapped to these regions. On the other hand, when the radar frequency is at 6.75 MHz, the second-order curve is not as distinct in the near-Bragg regions, implying less ocean spectral energy is mapped to the corresponding Doppler regions.

4. The Effects of Bistatic Angle

Figure 4.8 shows the radar cross sections as affected by different bistatic angles. The examining bistatic angles are set to be $\phi_0 = 0^\circ$, $\phi_0 = 30^\circ$, and $\phi_0 = 45^\circ$, respectively. In this figure the wind speed is $u_w = 10$ m/s, wind direction is $\theta_w = 0^\circ$, and the radar operation frequency is 15 MHz. While for the given variation in ϕ_0 , there is a nominal effect on the cross sections compared to the monostatic ($\phi_0 = 0^\circ$) case, it can be easily seen from equations (4.10) and (4.19) that the entire cross sections will be gradually reduced in magnitude as the bistatic angle ϕ_0 approaches 90° . Also, as ϕ_0 increases, the Bragg frequencies will decrease (see equations (4.14) and (4.15)).

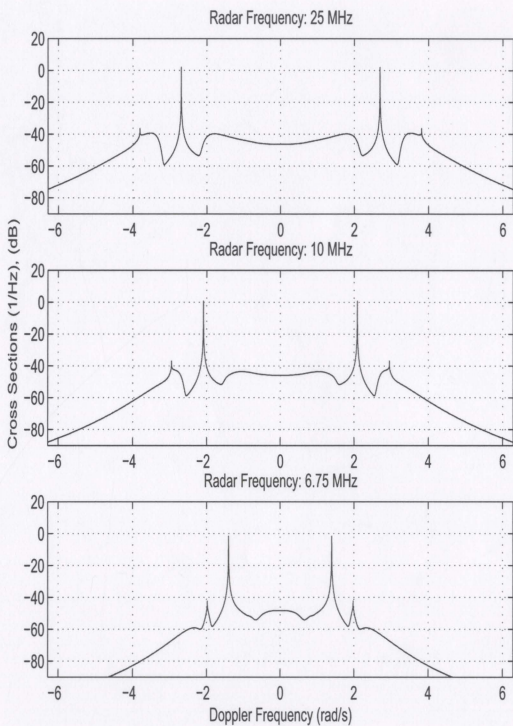


Figure 4.7: Bistatic cross sections for different radar frequencies. The bistatic angle is $\phi_0 = 45^\circ$. The wind velocity is 10 m/s, 0° to x -axis.

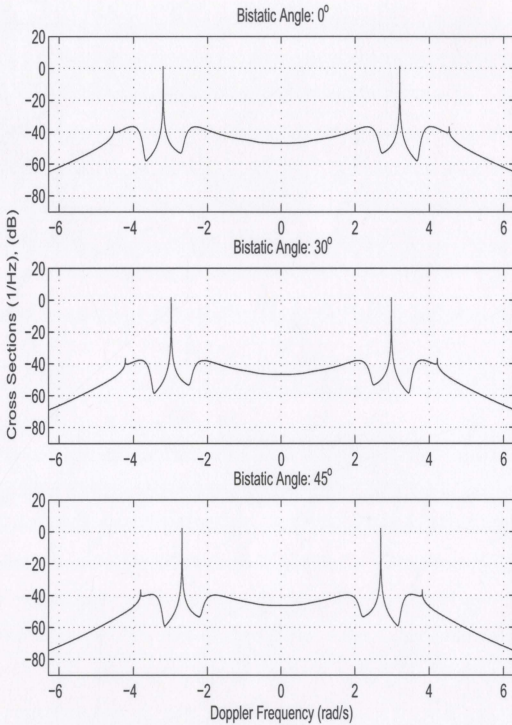


Figure 4.8: Bistatic cross sections for different bistatic angles. The radar operating frequency is 15 MHz, wind velocity is $u_w = 10$ m/s, 0° to the x -axis.

4.2 Time Series of Radar Return

The HF radar signals received from the ocean surface contain not only the useful ocean clutter but also unwanted noise. The strength of the radar received signal is a function of various parameters associated with the radar itself, including transmitted power, the gains of both the transmitter and receiver antennas, the distance from the radar transmitter to the scattering patch and the distance from scattering patch to the receiver and the radar operating frequency. Other factors affecting received signal strength include the size of the scattering patch, the attenuation function associated with the characteristics of the medium, and the ocean wave spectrum.

In the HF band, the reception is often externally noise limited. Here internal system noise will be ignored. The external noise in the radar system comes from a wide range of sources, such as atmospheric, galactic, and man-made noise. The noise depends on radar operating frequency, location, the season of the year, and the time of the day.

In Gill's analysis [15], the PSD of the ocean clutter and ambient noise are thoroughly investigated and a mathematical model is obtained to describe the received power from the ocean surface scatter. In this section, based upon Gill's model, the external noise is assumed to be a stationary Gaussian white process with zero mean. The PSDs of the ocean clutter and external noise are calculated separately in the frequency domain. An inverse transform of the PSDs to the time domain results in the radar received time series of clutter and noise, respectively. During the inverse transform, Pierson's [40] model of a stationary Gaussian process in one variable has been invoked. The motion of the ocean surface current has been inserted into the clutter time series. The combination of clutter and noise in the time domain gives the time series of the received signals. After further discussion a typical example is illustrated in Figure 4.11.

4.2.1 The PSD of Ocean Clutter

When pulsed radar is in operation and the scatter from the ocean surface is received via a narrow beam receiving system, the power spectral density of the ocean clutter, denoted as $P_c(\omega)$, can be written using the radar range equation [15] as

$$P_c(\omega) = \frac{\lambda_0^2 \left(\frac{\tau_0}{T_L}\right) P_t G_t G_r |F(\rho_{01}, \omega_0) F(\rho_{02}, \omega_0)|^2 A_r}{(4\pi)^3 \rho_{01}^2 \rho_{02}^2} \sigma(\omega) . \quad (4.25)$$

Here, the patch area A_r is defined as

$$A_r = \frac{c\tau_0\rho_{02}BW_{\frac{1}{2}}}{2} , \quad (4.26)$$

where $\frac{c\tau_0\rho_{02}}{2}$ is the width of scattering patch in the radar look direction and $BW_{\frac{1}{2}}$ is half beamwidth of the receiver antenna.

All the parameters in the radar range equation may be catalogued in two groups:

1. The parameters associated with the radar system: these include the transmitted pulse (peak) power P_t , the gains G_t and G_r of the transmitting and receiving antennas, respectively, the half beamwidth of the receiving antenna $BW_{\frac{1}{2}}$, the transmitting pulse width τ_0 , and the pulse repetition period T_L . $\frac{\tau_0}{T_L}$ is defined as the radar duty cycle. Figure 4.9 depicts an example of a pulse train.
2. The parameters associated with electromagnetic wave propagation and sea state: these include the distance ρ_{01} between the transmitter and scattering patch, the distance ρ_{02} between the scattering patch and receiver (Figure 2.4), the rough spherical earth attenuation function $F(\rho, \omega_0)$, and cross section $\sigma(\omega)$. $F(\rho, \omega_0)$ is a function of the radar operating frequency and the geometric relationship between the transmitter and the scattering patch and the scattering patch and receiver over the earth surface. For a bistatic radar configuration, we have $F(\rho_{01}, \omega_0)$ and $F(\rho_{02}, \omega_0)$

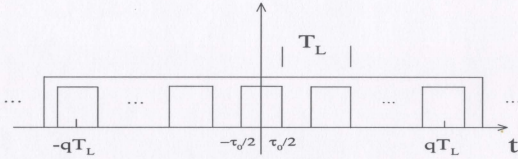


Figure 4.9: A pulse train with pulse width τ_0 and pulse repetition frequency T_L .

associated with radar operating frequency ω_0 and the distances of ρ_{01} and ρ_{02} , respectively. Strictly speaking, $F(\cdot)$ is also a function of sea state, and will decrease when sea state increases. Other relevant parameters include wind speed and direction, dielectric constant and permeability of the ocean surface. Dawe [41] has developed a Fortran routine to calculate this attenuation function.

The receiving antenna is assumed to be an N -element linear array with an element spacing of $d_s = \frac{\lambda_0}{2}$. The receive array beamwidth and receive array gain (assuming 100% efficiency) are defined by Collin [42] as

$$BW_{\frac{1}{2}} = \frac{2.65\lambda_0}{(N+1)\pi d_s} \quad (4.27)$$

and

$$G_r = \frac{5.48(N+1)d_s}{\lambda_0}, \quad (4.28)$$

respectively.

4.2.2 The PSD of Stationary Gaussian Noise

The description of the PSD of a stationary Gaussian white noise for sampling at the pulse centers can be found in Gill [15]. The external Doppler noise PSD, $P_N(\omega)$ is written as

$$P_N(\omega) = \frac{d_c k T_0}{2\pi} 10^{\left(\frac{F_{am}}{10}\right)} \sum_{L\left(-\frac{1}{2d_c}\right)}^{G\left(\frac{1}{2d_c}\right)} \text{Sa}[m\pi d_c] . \quad (4.29)$$

where $k = 1.38 \times 10^{-23}$ J/K is Boltzmann's constant and $T_0 = 290$ K is the reference temperature (Kelvins). Usually, an external noise figure F_{am} is available in documents such as *ITU-R Recommendations* [43]. The radar duty cycle $\frac{\tau_0}{T_L}$ has been replaced by d_c . The quantity $L\left(-\frac{1}{2d_c}\right)$ is defined as the smallest integer that is greater than or equal to $-\frac{1}{2d_c}$, and $G\left(\frac{1}{2d_c}\right)$ is the greatest integer that is less than or equal to $\frac{1}{2d_c}$ while $\text{Sa}(\cdot)$ is the usual sampling function. The equation (4.29) can be simplified under certain conditions. For example, for a typically small duty cycle, say 4%, the summation term in equation (4.29) will be close to unity. In such a case, there exists a closed form expression of the noise [43]:

$$(P_N(f))_{\text{dB}} = 10 \log P_N(f) = -204 \text{dB} + F_{am} \quad (4.30)$$

where frequency f is in hertz. Some typical values of the noise figure F_{am} as taken from [41] at frequencies 25 MHz, 10 MHz and 6.75 MHz are 22 dB, 36 dB, and 40 dB, respectively. They will result in the noise floors of PSDs around -180 dB, -170 dB, and -160 dB, correspondingly. Figure 4.10 shows a typical example of the PSD of external noise. Detailed analysis can be found in [15].

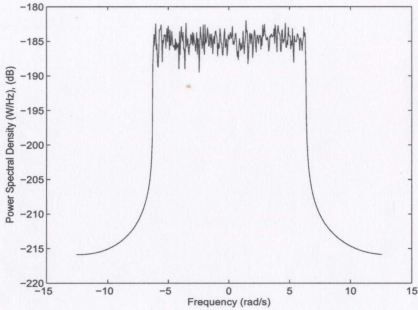


Figure 4.10: Power spectral density of external noise.

4.2.3 The Simulated Time Series

From equations (4.25) and (4.30) we have expressions for the PSDs of the ocean clutter and noise, respectively. In order to obtain simulated time series, the PSD of the clutter and noise, may be transferred to the time domain. The transform from frequency domain to time domain can be accomplished by employing Pierson's model [40] of a one-dimensional stationary Gaussian process. Gill [15] presents a time function $f(t)$ of limited bandwidth B to describe the ocean wave system as

$$f(t) = \int_B e^{j\omega t} e^{j\epsilon(\omega)} \sqrt{F_s(\omega)} \frac{d\omega}{2\pi}, \quad (4.31)$$

where $f(t)$ presents the time signal of either the noise $n(t)$ or ocean clutter $c(t)$, $F_s(\omega)$ is PSD of $f(t)$, and $\epsilon(\omega)$ is a random phase term uniformly distributed between $[0, 2\pi)$. This integral is calculated over the Doppler spectrum band B , where the frequency ω is

defined in the range

$$-\frac{B}{2} \leq \omega \leq \frac{B}{2}. \quad (4.32)$$

However, the integral of equation (4.31) cannot be calculated directly. A numerical routine presented by Pierson [40] allows the integral to be approximated as

$$f(t) = \lim_{\substack{\omega_{2p} \rightarrow \infty \\ (\omega_{2q+2} - \omega_{2q}) \rightarrow 0}} \sum_{q=0}^p e^{j(\omega_{2q+1}t)} e^{j\epsilon(\omega_{2q+1})} \sqrt{F_s(\omega_{2q+1}) \cdot \frac{\omega_{2q+2} - \omega_{2q}}{2\pi}}, \quad (4.33)$$

where q is a whole number. When $\omega_{2p} \rightarrow \infty$, the number of pulse trains extends to infinity. If $c(t)$ is denoted as the time series of ocean clutter and $n(t)$ is denoted as the time series of noise, the sum of the $c(t)$ and $n(t)$ will result in the signal $s(t)$. Thus, developing $c(t)$ and $n(t)$ from equation (4.33) allows the received signal to be simulated simply as

$$s(t) = c(t) + n(t). \quad (4.34)$$

Figure 4.11 is an example of such a simulation.

4.3 From Time Series to Vector Current

4.3.1 Introduction

If the radar pulse width and the antenna parameters for both sites are fixed, the ocean surface can be divided into different cells along the constant bistatic angle locus (see Figure 4.12 of Section 4.3.2). Measurements of vector current over each cell would be accomplished separately. Within each cell, the radial currents along the monostatic and bistatic radar look directions will be obtained independently and then vector currents

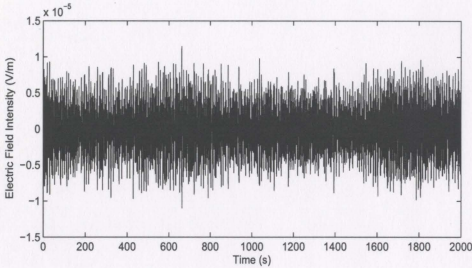


Figure 4.11: Example of radar received time series. Radar operating frequency is 25 MHz, wind velocity is 15 m/s, 90° to radar look direction.

will be derived by means of equations (2.26) and (2.27). The overall current map of the ocean surface can be extracted through such a series of “constant bistatic angles”.

For the purpose of simplicity in the simulation, the currents are first assumed to be uniformly distribution over the entire area. This means that as the scatter patch moves along the constant bistatic angle, the relative angles between the radar look directions (monostatic and bistatic) and the current direction are always changing. During this change the current projections along the two radar look directions are also varying. Carrying out the analysis, the algorithm of extraction of vector current by the combination of radial currents can be tested for different conditions. In the second test, the vector currents are estimated under the assumption of a non-uniform current distribution.

Centroids of the First-order Peak Regions

The centroid is defined as the frequency position that separates the first-order peak region into two portions with equal areas. A numerical procedure is used for locating the centroid presented by Bobby [23].

1. Locate the absolute maxima, ω_P and ω_N in the positive and negative Doppler ranges, respectively.
2. Locate the two nulls beside the negative Bragg peaks by calculating the average power over a range of frequencies falling within the two intervals that are known to include the nulls. Here, we choose intervals $-1.8 \omega_N$ to $-1.2 \omega_N$ and $-0.8 \omega_N$ to $-0.3 \omega_N$. Then, starting from ω_N , the nulls are determined as the first set of local values beside the ω_N that fall below the appropriate average.
3. To locate the nulls ω_P , repeat step 2 for the positive Doppler ranges in the intervals $1.2 \omega_P$ to $1.8 \omega_P$ and $0.3 \omega_P$ to $0.8 \omega_P$.
4. Find the centroid frequency for each side of the Doppler spectrum as that frequency value at which half of the entire area between two nulls is covered.

Considerations of the SNR

In developing the simulation results it is also important to address typical clutter signal to noise ratios (SNR). For pulse radar, this SNR is defined as

$$\text{SNR} = \frac{P_c(\omega)}{P_N(\omega)}, \quad (4.35)$$

where $P_c(\omega)$ is defined by the radar range equation (4.25) and $P_N(\omega)$ is the noise spectral density. SNR is simply the difference (in dB) between the maximum magnitude of the Bragg peaks and the noise floor. In our simulation, Gaussian white noise is used to simulate the noise floor [15]. In practice, it is necessary to set a SNR threshold in order to select useful data. All radar data below the SNR cutoff criterion is, of course, discarded.

Comparing the theoretical Bragg peaks with the centroid frequency positions, the difference can be identified and recognized as the consequence of currents. If the SNR of one side of the Doppler spectrum is below the threshold, the other side with SNR higher

than the threshold will be used to obtain the radial current component. If the SNRs of both sides are above the threshold, we have two options: One option is to use the average shift of the positive and negative peaks. The advantage of this approach is to diminish the effect of random noise fluctuations. The second option is to use only the side with the higher SNR. The advantage of this option is that only higher quality data are used in extracting the radial current. In this study, a combination of the two approaches is used. A 25 dB value is set and the magnitudes of the Bragg peaks of both sides are compared to each other. If their differences are less than that value, option one is applied; if the differences are larger than 25 dB, option two is chosen.

When radar data are picked up with SNRs higher than a certain value, the quality of results will not improve significantly. As an illustration of this idea, Hickey [22] checked two different SNRs, 10 dB and 30 dB for real data analyses of monostatically received signals. The statistical comparison of radial currents obtained from real data with 10 dB and 30 dB SNRs has shown little difference, which indicates that a SNR higher than 10 dB does not bring significant improvement to the results.

4.3.2 Simulation Details

In simulation, the transmitting antenna is an omnidirection antenna with 2 dBi transmitting gain. The receiving antenna is a 24 element linear array with half wavelength spacing and a gain of 18 dBi. The azimuthal extent of the patch, as determined by $BW_{\frac{1}{2}}$ (see equation (4.27)), is 4° and the radial extent is 1500 m. For each simulation, a 4096-point time series is taken from a specific radar direction. This time series is fast Fourier transformed in 512-point segments with a 50 percent overlap and square-averaged to yield the Doppler power spectral density. The sampling rate is chosen to be 0.25 s in the simulation. This corresponds to a 4 Hz sampling rate and 0.0039 Hz FFT resolution.

The radar coverage area is set up before the simulation is conducted. The effective

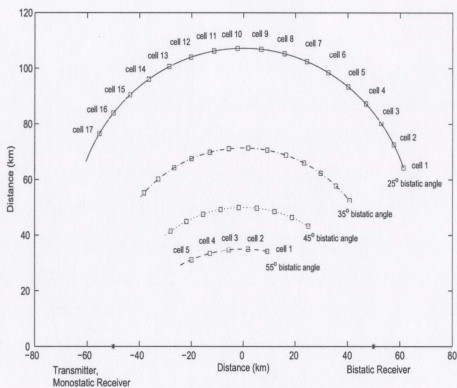


Figure 4.12: An illustration of cell number.

value of the GDOP is chosen to be less than 3.5, as indicated in Figure 3.2. This corresponds to a bistatic angle of approximately 23° . In the simulation, a region over the ocean surface in the middle between two receivers is chosen so that the bistatic angles vary from 25° to 55° .

The contour of the constant bistatic angle is shown in Figure 4.12. The scattering patches are chosen to move along the locus of constant bistatic angles of 55° , 45° , 35° , and 25° from front to rear, respectively. In this figure the scattering patches are shown as a series of cells with the cell numbers being counted from right to left as an example in the simulation. It is also assumed that the cells are from 30° to 150° (with respect to x -axis) with a 4° increment. Of course, there will be fewer patches along the constant bistatic angle locus when bigger bistatic angles are used. In fact, when the two radar receivers are fixed, the optimal surveillance area is established. On the other hand, in order to view a particular surveillance area the optimal positions for radar receivers must

be determined.

Figure 4.13 depicts an example where the vector current is measured with the radar operating frequency at 25 MHz, the bistatic angle set at 55° , and the location set to cell number four. The current is 1.2 m/s, 60° to the reference direction. The top two figures are the Doppler spectra obtained at monostatic and bistatic radar receivers without current, while in the two figures in the bottom the current is introduced. The Doppler shift effect is indicated by the dashed lines. In the example, the current component at the monostatic receiver is 1.141 m/s in the original, but the measured value is 1.148 m/s, while the current component of the original and measured values for the bistatic receiver are 0.958 m/s and 0.977 m/s, respectively. Using the measured values of the current components, the vector current can be derived (using equations (2.26) and (2.27)) as having a magnitude of 1.21 m/s, 60.67° to the reference direction, which is in good agreement with the original current.

4.3.3 Simulated Results for Uniformly Distributed Currents

To completely examine the algorithm, different combinations of radar operating frequencies and ocean current vectors should be tested. Radar frequencies of 25 MHz, 15 MHz, and 6.75 MHz will be used, corresponding to higher, middle and lower end in the HF band. Usually, the ocean surface current speeds are changed in the range from 0.15 m/s to 1.2 m/s. Several currents are picked in this range for illustration. Throughout the analysis, the errors of radial current components are within the FFT resolution.

Currents with same direction but different magnitudes measured by same radar frequency:

Figures 4.14 and 4.15 depict the results for a radar operating frequency at 25 MHz when the bistatic angles are 25° and 30° , respectively, and the current direction is 60° . Figures

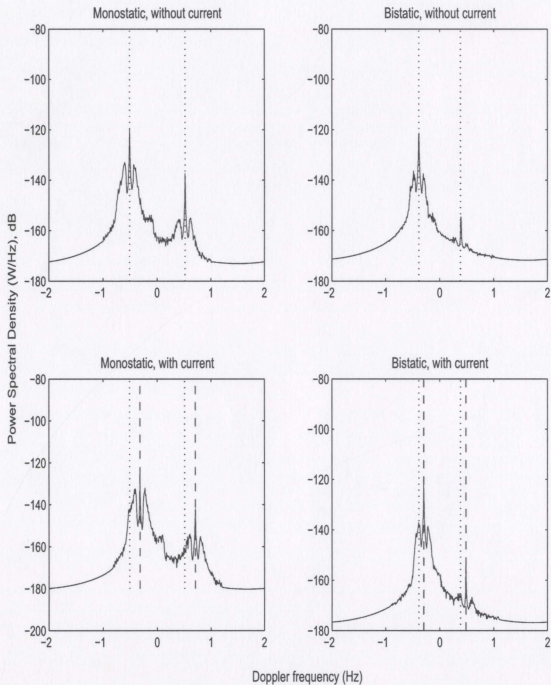


Figure 4.13: An example of radial currents measured from monostatic and bistatic radar directions. The radar operating frequency is 25 MHz, the bistatic angle is 55° , and the location of the ocean surface is at cell number four. The original current is 1.2 m/s, 60° to the reference direction. The dotted lines indicate the centroid frequencies of the Bragg peaks without the current, while the dashed lines show the Doppler shifted centroid positions of the Bragg peaks.

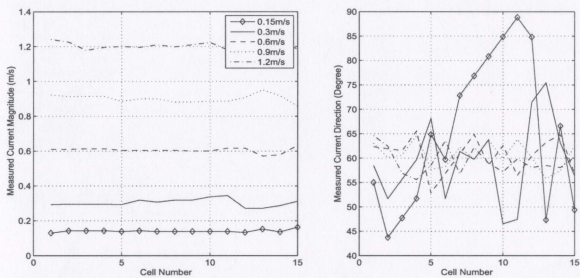


Figure 4.14: Results for different current magnitudes measured at 25 MHz. The bistatic angle is 25° . The magnitudes are selected as 0.15 m/s, 0.3 m/s, 0.6 m/s, 0.9 m/s, and 1.2 m/s. The current direction is 60° to the x -axis.

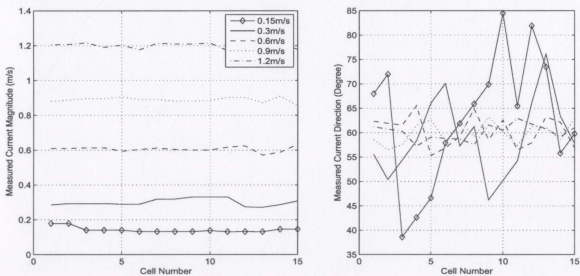


Figure 4.15: Results for currents with different magnitudes measured at 25 MHz. The bistatic angle is 30° . The other parameters are the same as in Figure 4.14.

4.16 and 4.17 depict the absolute errors of magnitude and direction in detail. It may be observed that the errors in magnitudes are not significant for any of the speeds used, but errors in measured directions increase when the original current magnitudes are small. In case of the 25° bistatic angle (Figure 4.14 and 4.16), the maximum measured errors in magnitude for these five original currents are all around 5 cm/s. However, the maximum error in current direction is 30.0° for the 0.15 m/s current, but only 4.5° for the 1.2 m/s current. Similar results occur in the case of the 30° bistatic angle (Figures 4.15 and 4.17).

Currents with same magnitude and direction measured by different frequencies:

Figure 4.18 shows a current of magnitude 0.9 m/s, 60° to the x -axis measured by the radar with operating frequency 25 MHz but with different bistatic angles 25° , 35° , 45° , and 55° , respectively. Figure 4.19 depicts the same current measurement with same radar operating frequency. It is observed that the measured results from 25 MHz are much better than that from 6.75 MHz. The maximum error in direction is less than 10° in 25 MHz but it is more than 20° in 6.75 MHz. For this same original current, the maximum error in magnitude with a radar operating frequency of 25 MHz is 8 cm/s, while for a radar frequency 6.75 MHz it is 12 cm/s.

4.3.4 Simulated Results for Non-uniform Current Pattern

The measurements involving variable currents are conducted by means of three different frequencies 6.75 MHz, 15 MHz, and 25 MHz, respectively. At each operating frequency, a distinct set of parameters is chosen. For 25 MHz the distance between the two receivers is selected as 45 km, while for 15 MHz this distance is 90 km, and for 6.75 MHz it is 180 km. The choice of different distances between the two receivers for different radar frequencies makes the simulation more realistic, since the lower the radar frequency the

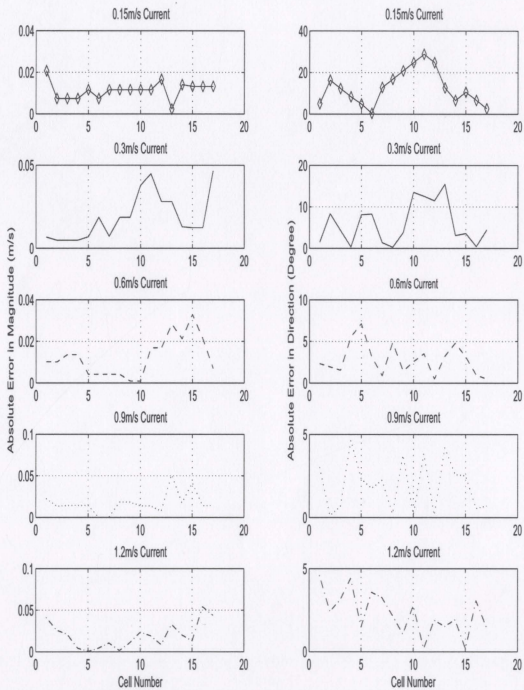


Figure 4.16: Absolute differences of the radial current components along the monostatic and bistatic directions measured at bistatic angle of 25° . The parameters are the same as in Figure 4.14.

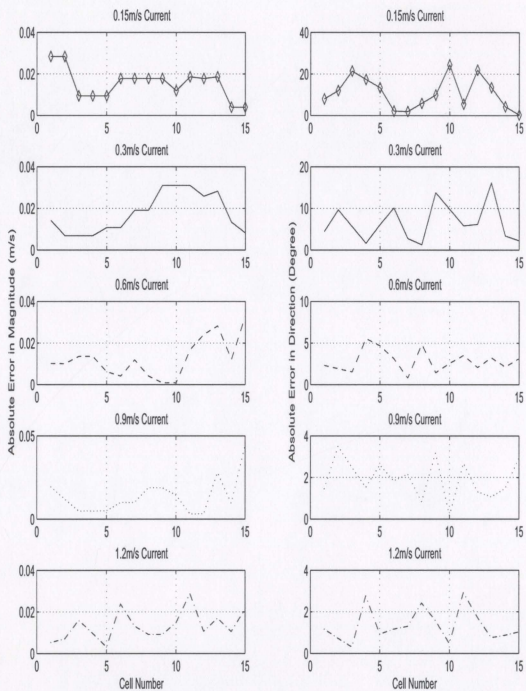


Figure 4.17: Absolute differences of the radial components along the monostatic and bistatic directions measured at bistatic angle of 30° . The parameters are the same as in Figure 4.15.

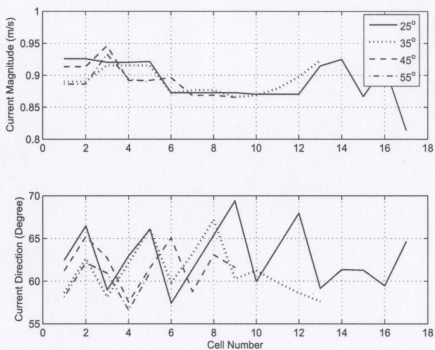


Figure 4.18: A current with 0.9 m/s, 60° to the x -axis is measured. The radar frequency is 25 MHz, bistatic angles are 25° , 35° , 45° , and 55° , respectively.

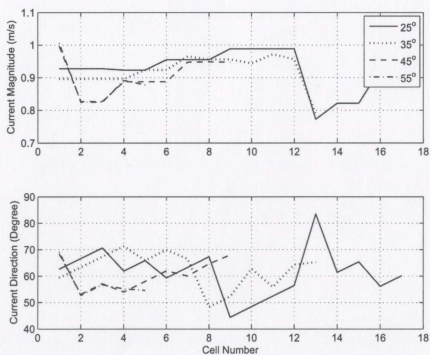


Figure 4.19: Same current as in Figure 4.18 is measured. The radar frequency is 6.75 MHz. The bistatic angles are chosen as in Figure 4.18.

further the e-m wave propagates over the ocean surface. The parameters used in the 25 MHz case are listed below as an example.

1. Radar operating frequency: 25 MHz.
2. Transmitting power: 100 W.
3. Transmitting antenna gain: 2 dBi.
4. Receiving antenna gain: 18 dBi.
5. Pulse width: 13.3 μ s.
6. Pulse repetition time: 333 μ s.
7. Distance between two receivers: 45 km.
8. receive array half-power beam width: 4.03° assuming 24 elements linear array, broadside.
9. Sampling rate: 4 Hz.
10. FFT resolution: 0.0039 Hz.
11. Radial current resolution along monostatic direction: 2.4 cm/s.
12. Radial current resolution along bistatic direction: from 2.7 cm/s to 4.2 cm/s depending upon different bistatic angles.

The simulated results are illustrated in Figure 4.20 with the top-left subplot giving the original current as varying magnitude from 0.8 m/s to 1.0 m/s and in direction from 30° to 300°. Figures 4.21 to 4.24 illustrate the absolute errors in magnitude and direction for the simulated currents at bistatic angles of 25°, 35°, 45°, and 55°, respectively.

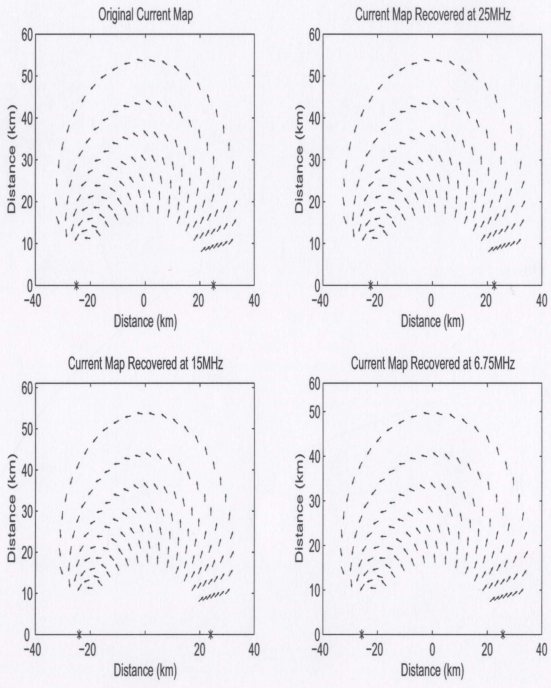
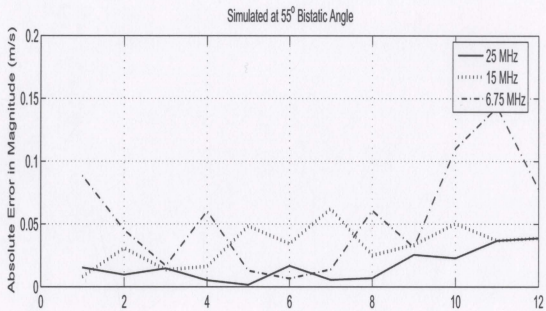
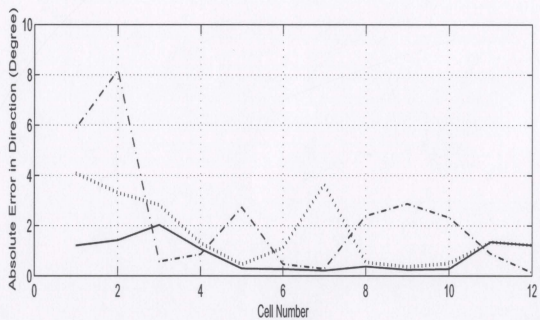


Figure 4.20: The comparisons of original current maps and current maps simulated at 25 MHz, 15 MHz, and 6.75 MHz, respectively.

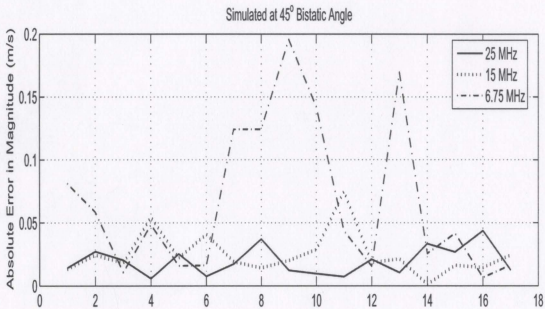


(a)

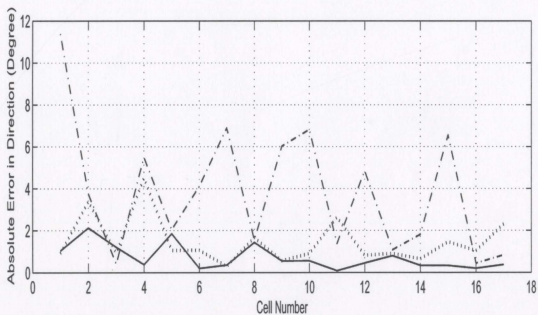


(b)

Figure 4.21: The absolute errors in (a) magnitude and (b) direction for the simulated currents at a bistatic angle of 55° . The radar operating frequencies are 25 MHz, 15 MHz, and 6.75 MHz, respectively.

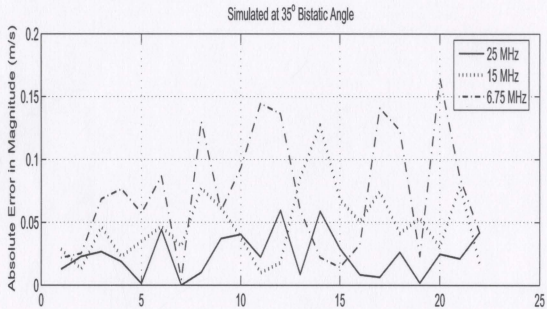


(a)

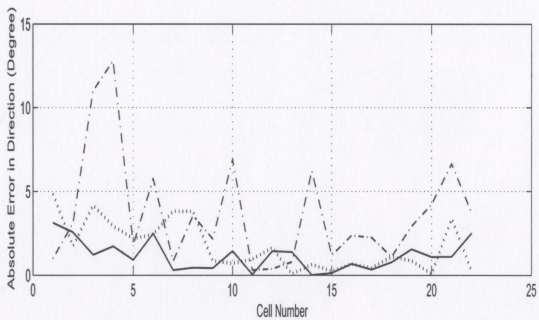


(b)

Figure 4.22: The absolute errors in (a) magnitude and (b) direction for the simulated currents at a bistatic angle of 45°. The radar operating frequencies are the same as in Figure 4.21.

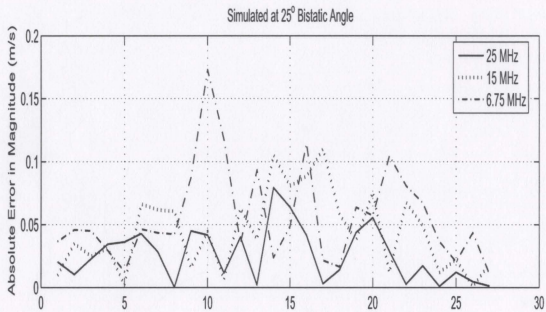


(a)

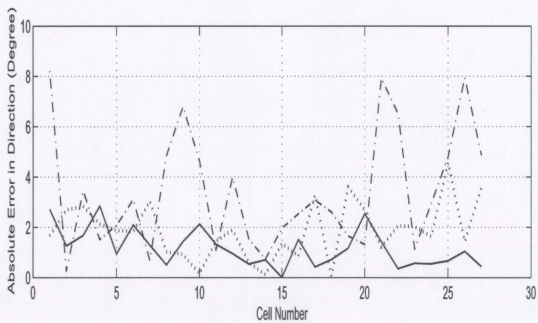


(b)

Figure 4.23: The absolute errors in (a) magnitude and (b) direction for the simulated currents at a bistatic angle of 35° . The radar operating frequencies are the same as in Figure 4.21.



(a)



(b)

Figure 4.24: The absolute errors in (a) magnitude and (b) direction for the simulated currents at a bistatic angle of 25°. The radar operating frequencies are the same as in Figure 4.21.

Bistatic angle ϕ_0 (Degree)	Maximum error (cm/s)		
	25 MHz	15 MHz	6.75 MHz
25	7.6	11.0	17.3
30	6.4	12.3	32.5
35	6.0	12.7	16.5
40	3.9	6.5	23.1
45	4.4	7.4	19.6
50	3.2	6.4	18.9
55	3.9	6.0	13.4

Table 4.1: Maximum errors in current magnitude.

Bistatic angle ϕ_0 (Degree)	Maximum error (Degree)		
	25 MHz	15 MHz	6.75 MHz
25	2.84	4.57	8.20
30	2.41	3.96	8.33
35	3.13	5.85	12.8
40	2.54	4.07	8.94
45	2.13	4.50	11.4
50	2.22	3.37	7.70
55	2.03	4.08	8.18

Table 4.2: Maximum errors in current direction.

Tables 4.1 and 4.2 summarize the maximum errors of measurements in the simulation both in magnitudes and directions for bistatic angles from 25° to 55° in 5° steps, corresponding to the results in Figure 4.20.

From the above simulations we conclude that:

1. The configuration of a pair of bistatic and monostatic receivers sharing the same transmitter has the potential to measure the ocean surface vector current. At the lower HF band, the errors in the radial current tend to increase and as the consequence, the accuracy in the vector current, both in direction and magnitude, will decrease accordingly. Therefore, to achieve a good accuracy for a limited integration time, it is better to choose a higher frequency in HF band.

2. According to analysis in the Chapter 3, if the bistatic angle of the radar configuration has been chosen adequately to keep the values of GDOP lower than a certain threshold, the error of the combined current vector will be moderate and acceptable. In our analysis, the range of the useful bistatic angle has been chosen within 25° to 55° .
3. For the same operating frequency, the original current speed does not appreciably influence the accuracy of measurement of the current magnitude but it does affect the accuracy of direction significantly.

Chapter 5

Conclusions

5.1 General Summary

HF radar wavelengths are similar in scale to ocean gravity waves that contain significant ocean energy. Furthermore, these signals have the ability to propagate over the horizon across the ocean surface. Thus, HF radar is becoming one of the most useful technologies for measuring surface parameters over large expanses of ocean. The algorithm developed here for current measurement by means of two separately located radar receivers, one of them co-located with a radar transmitter and another several kilometers from the transmitter, demonstrates encouraging results. We expect an examination of the validity of the algorithm in future field experiments.

The algorithm is developed based on theoretical models for HF bistatic radar cross sections of the ocean surface [13] and techniques for current measurement addressed by numerous investigators over several decades (see, for example, [2],[3],[6],[20],[22],[44],[23], and [27]). The successful development of the algorithm will enhance the capabilities of land-based HF radars and provide the basis of operation of more flexible, compact, and economically feasible systems. Below is a brief list of considerations in current measurements and the suggestions for the future research work.

In order to apply the bistatic radar in current measurement, the existing HF radar current measurement techniques have been reviewed in Chapter 2, and the geometrical configuration of a combined monostatic/bistatic radar vector measurement system has been introduced. The advantages and the disadvantages between this system and other systems, especially the dual-radar system, are discussed. It has been pointed out that the bistatic angle ϕ_0 plays important roles in the description of the bistatic radar received cross section and the extraction of the vector current measurement when the combined radar system is used.

The errors in current measurements have been analyzed in Chapter 3. These errors originate at the stage where the radial current components are derived and show a complicated behavior when these components are combined to give the vector current. Throughout the analysis the FFT error has been used as the error of the radial current. The behavior of the error in the vector current has been described numerically, with an idea similar to the GDOP in the GPS system. Several cases have been simulated and analyzed. These include the errors in the radial current measurement with different magnitudes and directions, different bistatic angles of the combined radar system, and the different relative directions between radar look directions and the current directions.

It is seen that the errors in the derived current vector vary within a parallelogram defined by the bistatic angle of the radar system and the measuring resolutions on both sides of the radar look directions. The diagonals of the parallelograms are generally different in length. When the measured current is between two radar look directions, the variation in magnitude is determined by the shorter diagonal, whereas the variation in direction is determined by the longer diagonal. These shows a better measurement in magnitude than in direction. On the other hand, when the current directions are outside the radar look directions, the variation of magnitude is determined by the longer diagonal and variation of direction is determined by the shorter one, corresponding to a

better measurement in current direction than in magnitude.

In Chapter 4, the vector current has been measured for simulated data. The first- and second-order radar cross sections are reviewed and the time series of the radar received data by the monostatic and bistatic radar receivers are simulated with current information inserted and Gaussian noise added. The radar Doppler spectra on both radar look directions are estimated by means of the periodogram method. The centroid frequencies of the Bragg peak regions are calculated and the radial current speeds are derived. Finally, both uniform and non-uniform vector currents have been input and the resulting currents have been extracted. Comparisons of the results with the input currents have shown good agreement, indicating the validity of the algorithm.

5.2 Suggestions for Future Work

Several points may be suggested for further research and experimental work. First, although the algorithm shows encouraging results, it still needs to be checked against real data. Since the HF radars have already been installed at Cape Race and Cape Bonavista, NL, Canada, we may have opportunity to perform such an examination in the near future. Furthermore, plans to develop smaller systems for deployment in Placentia Bay, NL are ongoing. Such systems could indeed be dedicated to validating the analysis and results presented in this work.

Some parametric spectral estimation methods have been reported in HF radar data analysis and the results are encouraging. However, the periodogram method is widely used in practice and theory. It would be a good idea to compare the advantages and disadvantages among different methods in future research.

An immediate next step along this research is the development of an algorithm in which two bistatic radar receivers are used. In such a system, two radar receivers would be located several kilometers away and on each side of the radar transmitter. The distances

from both receivers to the transmitter may or may not be equal. Actually, this idea may be extended to include more receivers and transmitters — i.e. the bistatic configuration may be extended to the multi-static case. This may provide more flexibility in the surveillance area for current measurements and improve the efficiency of data usage by sharing data among more receivers. Any such advances will continue to enhance the utility of HF radars as ocean remote sensors.

Bibliography

- [1] E. Shearman, "Radio science and oceanography," *Radio Science*, vol. 18, no. 3, pp. 299-320, 1983.
- [2] D. Crombie, "Resonant backscatter from the sea and its application to physical oceanography," in *Oceans '72 Conf. Rec.*, (IEEE Publ. No. 72CHO 660-1 OCC), pp. 173-179, 1972.
- [3] R. Stewart and J. Joy, "HF radio measurements of surface currents," *Deep-Sea Research*, vol. 21, pp. 1039-1049, 1974.
- [4] D. Barrick, J. Headrick, R. Bogle, and D.D.Crombie, "Sea backscatter at HF: interpretation and utilization of the echo," in *Proceedings of the IEEE*, vol. 62, pp. 673-680, 1974.
- [5] Antenna Standards Committee of the IEEE Antennas and Propagation Society, The Institute of Electrical and Electronics Engineers Inc., New York, *IEEE Standard Definitions of Terms for Antennas*, 145-1983 ed., 1983.
- [6] D. Barrick, "First-order theory and analysis of MF/HF/VHF scatter from the sea," *IEEE Transactions on Antennas and Propagation*, vol. 20, pp. 2-10, 1972.
- [7] S. Rice, "Reflection of electromagnetic waves from a slightly rough surface," in *Theory of Electromagnetic Waves* (K. Kline, ed.), pp. 351-378, New York: Interscience, 1951.

- [8] D. Barrick, "Remote sensing of sea state by radar," in *Remote Sensing of the Troposphere* (V. Derr, ed.), ch. 12, pp. 1-46, Washington, DC: U.S. Government Printing Office, 1972.
- [9] D. Barrick and B. Lipa, "The second-order shallow water hydrodynamic coupling coefficient in interpretation of HF radar sea echo," *IEEE J. Oceanic Eng.*, vol. 11, no. 2, pp. 310-315, 1986.
- [10] J. Walsh, "On the theory of electromagnetic propagation across a rough surface and calculations in the VHF region," OEIC Report N00232, Memorial University of Newfoundland, St. John's, Newfoundland, 1980.
- [11] S. Srivastava, *Analysis of HF scattering from an ocean surface: An alternative approach incorporating a dipole source*. PhD thesis, Memorial University of Newfoundland, St. John's, Newfoundland, 1984.
- [12] J. Walsh, R. Howell, and B. Dawe, "Model development for evaluation studies of ground wave radar," Contract Report 90-C14, Centre for Cold Ocean Resources Engineering, 1990. (Prepared for Department of National Defence, Government of Canada, DSS Contract Number W7714-8-5655/01-SS).
- [13] E. Gill and J. Walsh, "High-frequency bistatic cross sections of the ocean surface," *Radio Science*, vol. 36, no. 6, pp. 1459-1475, 2001.
- [14] E. Gill, W. Huang, and J. Walsh, "On the development of a second-order bistatic radar cross section of the ocean surface: A high frequency result for a finite scattering patch," *IEEE J. Oceanic Eng.*, vol. 31, no. 4, pp. 740-750, 2006.
- [15] E. Gill, *The Scattering of High Frequency Electromagnetic Radiation from the Ocean Surface: An Analysis Based on a Bistatic Ground Wave Radar Configuration*. PhD thesis, Memorial University of Newfoundland, St. John's, Newfoundland, 1999.

- [16] Wave Propagation Laboratory, Boulder, Colorado, USA, *Coastal Ocean Dynamics Applications Radar—A user's Guide*, 1984.
- [17] K. Gurgel, G. Antonischki, H. Essen, and T. Schlick, "Wellen radar (WERA): a new ground-wave HF radar for ocean remote sensing," *Coastal Engineering*, vol. 37, pp. 219–234, 1999.
- [18] C. Teague, "Multi-frequency HF radar observations of currents and current shears," *IEEE J. Oceanic Eng.*, vol. OE-11, no. 2, pp. 258–269, 1986.
- [19] L. Wyatt and J. Ledgard, "OSCR wave measurements—some preliminary results," *IEEE J. Oceanic Eng.*, vol. 21, no. 1, pp. 64–76, 1996.
- [20] L. Shay, T. Cook, H. Peters, A. Mariano, R. Weisberg, P. An, A. Soloviev, and M. Luther, "Very high-frequency radar mapping of surface currents," *IEEE J. Oceanic Eng.*, vol. 27, no. 2, pp. 155–169, 2002.
- [21] K. Butt, P. Jeans, and K. Hickey, "HF radar technology transfer project: implementation and testing of a two-site capability," Contract Report 83-11, Centre for Cold Ocean Resources Engineering, St. John's, Newfoundland, 1983.
- [22] K. Hickey, "Ocean surface current estimation using a long-range, single-station, high-frequency ground wave radar," Master's thesis, Memorial University of Newfoundland, St. John's, Newfoundland, 1999.
- [23] P. Bobby, "Estimation of vector surface currents beyond the region of overlap of dual-site HF radar: An implementation of the continuity equation," Master's thesis, Memorial University of Newfoundland, St. John's, Newfoundland, 2003.
- [24] A. Frisch and J. Leise, "A note on using continuity to extend HF radar surface-current measurements," *Journal of Geophysical Research*, vol. 86, no. 11, pp. 11089–11090, 1981.

- [25] D. Crombie, "Doppler spectrum of sea echo at 13.56 mc./s.," *Nature*, vol. 175, pp. 681–682, 1955.
- [26] B. Kinsman, *Wind Waves*. N. J.: Prentice-Hall, 1965.
- [27] B. Lipa and D. Barrick, "Least-squares methods for the extraction of surface currents from CODAR crossed-loop data: Application at ARSLOE," *IEEE J. Oceanic Eng.*, vol. OE-08, no. 4, pp. 226–253, 1983.
- [28] D. M. Fernandez, *High-Frequency Radar Measurements of Coastal Ocean Surface Currents*. PhD thesis, Stanford University, California, USA, 1993.
- [29] R. D. Chapman, L. K. Shay, H. C. Graber, J. B. Edson, A. Karachintsev, C. L. Trump, and D. B. Ross, "On the accuracy of HF radar surface current measurements: Intercomparisons with ship-based sensors," *J. Geophys. Res.*, vol. 102, no. 8, pp. 18737–18748, 1997.
- [30] J. Proakis, *Algorithms for Statistical Signal Processing*, vol. 3. New Jersey: Prentice-Hall, 2002.
- [31] N. Levanon, "Lowest GDOP in 2-D scenarios," in *Proceedings of the IEEE*, vol. 147, pp. 149–155, 2000.
- [32] B. Kinsman, *Wind Waves*. New York: Dover Publications Inc., 1984.
- [33] W. Pierson and L. Moskowitz, "A proposed spectral form for fully developed seas based upon the similarity theory of S.A. Kitaigorodskii," *J. Geophys. Res.*, vol. 69, no. 24, pp. 5181–5190, 1964.
- [34] M. Tucker, *Waves in Ocean Engineering*. New York: Ellis Horwood, 1991.
- [35] B. Lipa and D. Barrick, "Extraction of sea state from HF radar sea echo: Mathematical theory and modeling," *Radio Science*, vol. 21, no. 1, pp. 81–100, 1986.

- [36] R. Howell, "An algorithm for the extraction of ocean wave spectra from narrow beam HF radar backscatter," Master's thesis, Memorial University of Newfoundland, St. John's, Newfoundland, 1990.
- [37] P. E. Dexter and S. Theodorides, "Surface wind speed extraction from HF sky-wave radar doppler spectra," *Radio Science*, vol. 17, no. 3, pp. 643-652, 1982.
- [38] W. Huang, S. W. E. Gill, B. Wen, and J. Hou, "HF radar wind and wave measurement over the eastern china sea," *IEEE Trans. Geoscience Remote Sensing*, vol. 40, no. 9, pp. 1950-1955, 2002.
- [39] D. Green and E. Gill, "Extracting wind parameters from high frequency ground wave radar backscatter," in *IEEE AP-S International Symposium and USNC/URSI National Radio Science Meeting*, (Washington, DC, USA), 2005.
- [40] W. Pierson, "Wind generated gravity waves," *Advances in Geophysics*, vol. 2, pp. 93-178, 1955.
- [41] B. Dawe, "Radio wave propagation over earth: Field calculations and an implementation of the roughness effect," Master's thesis, Memorial University of Newfoundland, St. John's, Newfoundland, 1988.
- [42] R. Collin, *Antennas and Radio Wave Propagation*. New York: McGraw-Hill Book Company, 1985.
- [43] International Telecommunications Union, Geneva, *Propagation in Ionized Media (ITU-R Recommendations, 1994 PI Series Volume)*, 1994.
- [44] D. Barrick and B. Lipa, "A compact transportable HF radar system for directional coastal wavefield measurements," in *Ocean Wave Climate* (M. D. Earle and A. Malahoff, eds.), pp. 153-201, New York: Plenum, 1979.

